UC Irvine
UC Irvine Electronic Theses and Dissertations

Title
Phat ELVIS: The Inevitable Effect of the Milky Way's Disk

Permalink
https://escholarship.org/uc/item/3425r68q

Author
Kelley, Tyler

Publication Date
2019

Peer reviewed|Thesis/dissertation

eScholarship.org Powered by the California Digital Library
University of California

UNIVERSITY OF CALIFORNIA,
IRVINE

Phat ELVIS: The Inevitable Effect of the Milky Way's Disk

DISSERTATION

submitted in partial satisfaction of the requirements
for the degree of

DOCTOR OF PHILOSOPHY

in Physics

by

Tyler Evan Kelley

Dissertation Committee:
Professor James S. Bullock, Chair
Professor Michael C. Cooper
Professor Manoj Kaplinghat

2019

Chapter 1 © 2019 Oxford University Press
Chapter 2 © 2019 Oxford University Press
All other materials © 2019 Tyler Evan Kelley

DEDICATION

To

Alyssa

You will forever be my greatest adventure.

TABLE OF CONTENTS

Page

LIST OF FIGURES **iv**

LIST OF TABLES **vii**

ACKNOWLEDGMENTS **viii**

CURRICULUM VITAE **ix**

ABSTRACT OF THE DISSERTATION **xi**

1 Introduction **1**

2 Phat ELVIS: The inevitable effect of the Milky Way's disk on its dark matter subhaloes **5**

2.1 Simulations 5
2.1.1 Embedded Potentials 10
2.2 Results 14
2.2.1 Velocity Functions 16
2.2.2 Radial Distributions 17
2.2.3 Pericenter Distributions 19
2.2.4 Infall Times 20
2.2.5 Time Evolution of Substructure Counts 21
2.3 Implications 22
2.3.1 What haloes host ultra-faint galaxies? 22
2.3.2 Satellite Pericenters 29
2.3.3 Effects of Different Models 31
2.4 Discussion and Conclusions 31
2.4.1 Impact of the Disk on substructure populations 32
2.4.2 Numerical Convergence 33
2.4.3 Resolution Analysis 34
2.4.4 Observable consequences 35

Bibliography **39**

LIST OF FIGURES

Page

2.1 Visualization of the dark matter for Kentucky (left) and Kentucky `Disk` (right). The top panels span 500 kpc, approximately the virial volume of this halo. The bottom panels span 100 kpc. The absence of substructure at small radii in the `Disk` runs is striking. An enhancement in central dark matter density is also seen in the `Disk` runs, which is a result of baryonic contraction. The disk potentials are oriented face-on in these images. 9

2.2 Cumulative V_{max} (left) and V_{peak} (right) distributions for subhaloes within $R = 300$, 100, and 50 kpc (top to bottom) for all 12 of our DMO (black) and DMO+`Disk` runs (magenta). The solid lines are medians while the shaded bands span the full extent of the distributions. Note that the roll-off at low $V_{\rm peak}$ in the right panels are signatures of incompleteness. The $V_{\rm peak}$ completeness limit gets worse as we approach the halo centers (where stripping is more important). The simulations appear reasonably complete to $V_{\rm peak} \simeq 5 \mathrm{km\,s^{-1}}$ within 300 kpc. This limit drops to $V_{\rm peak} \simeq 6\ \mathrm{km\,s^{-1}}$ within 50 kpc. There is no such roll-off in $V_{\rm max}$, which suggests we are complete down to $V_{\rm max} \simeq 4.5\ \mathrm{km\,s^{-1}}$ throughout the haloes. 11

2.3 Cumulative counts for subhaloes within a given radius of the host. The black dashed lines represent the dark matter only runs and the magenta lines represent the same haloes with an embedded MW-like potential. Left: subhaloes with $V_{\rm max} > 4.5\ \mathrm{km\,s^{-1}}$. Right: subhaloes with $V_{\rm peak} > 10\ \mathrm{km\,s^{-1}}$. Note that the vertical axis scales are significantly different on the left and right. 12

2.4 Mass growth of the galaxy for Kentucky with scale factor. The individual components' growths as well as the total galaxy mass growth. The final ($a = 1$) position of all galaxy lines (not the dark matter halo virial mass) is fixed for all hosts as discussed in section 2.1.1. The dashed line near the top of the figure shows the halo's virial mass evolution. 15

2.5 Distribution of the pericentric distances for all surviving subhaloes with $V_{\rm max} > 4.5\ {\rm km\,s^{-1}}$ within a present-day radius of $R = 100$ kpc. The dashed and solid lines represent the subhalo distributions for individual host haloes in DMO and `Disk` runs, respectively. The lines are colored according to host halo mass as indicated by the color bar on the right. We do this to provide a way to help match haloes from one run to the next, not because there is any apparent trend with halo mass. The thick lines show median relations for their respective simulation type. Note that the `Disk` runs preferentially deplete subhaloes that have pericenters smaller than $\sim 20-30$ kpc. While the DMO simulations have pericenter distributions that spike towards zero, subhaloes in the `Disk` runs have pericenter distributions that peak at ~ 35 kpc. 18
2.6 Distributions of infall times when subhaloes first crossed into the host virial radius. Shown are distributions for all surviving subhaloes with $V_{\rm max} > 4.5\ {\rm km\,s^{-1}}$ within $R = 300$ kpc (left) and $R = 100$ kpc (right) stacked together for all of the DMO (gray) and `Disk` (magenta) simulations in our suite. The `Disk` runs are clearly depleted in subhaloes that fell in more than ~ 6 Gyr ago compared to the DMO runs, and especially so in the $R < 100$ kpc sample. 19
2.7 Number of subhaloes with $V_{\rm max} > 4.5\ {\rm km\,s^{-1}}$ that exist within 20 kpc (physical) of the host halo center as a function of lookback time. The gray and magenta distributions represent the distributions for the DMO and `Disk` runs, respectively. The solid lines show medians and the bands cover the full spread of the data. The difference between the two classes of runs persists back to 8 Gyr. 23
2.8 Median cumulative radial counts of subhalos for all of the `Disk` runs color coded by $V_{\rm peak}$ threshold. The faint gray lines mark $V_{\rm peak}$ thresholds larger than 7, 10, 15, and 20 ${\rm km\,s^{-1}}$, respectively. Thick lines represent the Milky Way satellite data uncorrected (red dashed) and corrected for sky coverage (solid black). The vertical dotted line at 40 kpc represents an estimate of the radial completeness limit for $L \simeq 1000\ {\rm L_\odot}$ ultra-faint dwarfs. Observed counts to the right of this line should be treated as lower limits, as the true counts may be much higher than those shown given the lack of a deep, full sky survey. If our host halos are representative of the Milky Way, then we must populate all subhaloes with $V_{\rm peak} \gtrsim 7\ {\rm km\,s^{-1}}$ in order to account for the data. This extrapolates to an implied total of ~ 1000 ultra-faint satellites within 300 kpc. 24
2.9 Median radial profiles for different $V_{\rm peak}$ cuts for all of the DMO runs. Compare to the `Disk` simulations shown in Figure 2.8. The faint gray lines represent the DMO data for fixed $V_{\rm peak}$ thresholds of 7, 10, 15, and 20 ${\rm km\,s^{-1}}$, respectively. The thick lines represent the Milky Way satellite data uncorrected (red dashed) and corrected for sky coverage (solid black). Haloes with $V_{\rm peak} \gtrsim 12\ {\rm km\,s^{-1}}$ are required to match the inner data in the median of our DMO runs, and this extrapolates to an implied total of ~ 200 ultra-faint satellites within 300 kpc. 25

2.10 Comparison of the pericenter distributions for subhaloes (black) with $V_{\max} > 4.5\ \mathrm{km\,s^{-1}}$ to those of the 21 MW satellites (red) within 100 kpc of the Galactic center as derived by Fritz et al. (2018). In order to account for radial completeness bias in the data, the subhaloes have been resampled to have the same $z = 0$ radial distribution as the data. Each host halo is weighted equally. Left: Differential DMO (dashed) and `Disk` (solid) median pericenter distributions with the MW satellite pericenter distribution shown in red. The gray bands represent the 95% confidence interval obtained from sampling the subhaloes pericenter distributions. Right: Cumulative pericenter distributions. The band represents the 95% confidence interval obtained from sampling the MW satellite pericenter values given their respective errors. Unlike the real MW satellites, the DMO subhaloes peak towards small pericenter. The `Disk` runs produce a subhalo pericenter distribution that is closer to the distribution seen in the data. 27

2.11 Differential pericenter distributions for subhaloes (black) with $V_{\max} > 4.5\ \mathrm{km\,s^{-1}}$ (left) and $V_{\mathrm{peak}} > 7\ \mathrm{km\,s^{-1}}$ (right) and MW satellites derived from both potentials used in Fritz et al. (2018). The pericenters derived using the "Light" MW potential are shown by the red line and is the same as figure 2.5 while those derived using the "Heavy" MW potential are shown by the blue line. The gray bands represent the 95% confidence interval for the subhaloes' distributions. 32

2.12 Comparison of the subhalo counts of the Hound Dog host halo from our fiducial (High, black) run to a lower resolution run (Low, red), with 64× fewer particles. The left panel shows a cumulative count of all subhaloes above a given $V_{\max}$, within 50 kpc of the host center. The right panel is similar but includes subhaloes out to 300 kpc. The vertical dotted line indicates where we would expect convergence ($V_{\max} = 15\ \mathrm{km\,s^{-1}}$) by scaling our adopted completeness threshold for the fiducial high-resolution runs ($V_{\max} = 4.5\ \mathrm{km\,s^{-1}}$). 35

2.13 Radial radial distributions of subhaloes with $V_{\max} > 15\ \mathrm{km\,s^{-1}}$ for the Hound Dog host halo from the fiducial resolution (High, black) and a run with 64× fewer particles (Low, red). Runs with Milky Way potentials `Disk` are shown as the dashed lines. The counts agree to within expected Poisson variation for both types of runs at all radii. 36

LIST OF TABLES

Page

2.1 Parameters for the Milky Way potential components at $z = 0$ used in every `Disk` run. The disk scale radii correspond to exponential disk radii, which we model analytically by summing three Miyamoto & Nagai (1975) disk potentials following Smith et al. (2015). The buldge radius corresponds to the scale radius of a Hernquist (1990) potential. Parameters were taken from McMillan (2017) and Bland-Hawthorn & Gerhard (2016). 6

2.2 Discography of halo properties at $z = 0$. Haloes are listed in pairs corresponding to DMO (first) and those run with embedded galactic potentials (second, designated '`Disk`'). The remaining columns list the Bryan & Norman (1998) virial mass, virial radius, maximum circular velocity, $V_{\rm max}$, and virial velocity ($\sqrt{GM_{\rm v}/R_{\rm v}}$), along with the the total number of subhaloes with $V_{\rm max} > 4.5\,{\rm km\,s^{-1}}$ that survive to $z = 0$ within 25, 50, 100, and 300 kpc of the halo center, the concentration based off of a best fit NFW, and the redshift at which the host obtained 50% of its final mass. 7

ACKNOWLEDGMENTS

First and foremost, I would like to thank my advisor, James Bullock. His support and mentorship for the past 5 years has significantly impacted my professional and scientific development. Without his guidance I would not be where I am today and could not have completed this program.

I could not have completed this without the support of my amazing wife, Alyssa. You helped motivate me and cheer me on when things were tough and ensured that I was well fed and, less often than you wanted, well-rested.

I would like to thank my committee members, Michael Cooper and Manoj Kaplinghat, for their support during graduate school. I would like to thank many co-authors (not listed above) who have greatly contributed to this work and my graduate student career, Shea Garrison-Kimmel, Mike Boylan-Kolchin, Andrew Graus, Victor Robles, and Marcel Pawlowski. I would like to thank Sean Fillingham whose educational stories and straightforward manner were very much appreciated.

Finally, I would like to thank my parents for all their love and support through these many years. The older I get the more I realize how much you have sacrificed to allow me to pursue my interests and shaped me into who I am today. My grandparents who encouraged me to reach for the stars and have always reminded me that my attitude is the one thing I get to choose, I love you to the moon and back.

The majority of this dissertation has been published in the Oxford University Press. Specifically, Chapter 2 was published in the Monthly Notices of the Royal Astronomical Society (MNRAS) 487 4409 (Kelley et al., 2019). This work was supported in part by NSF grants AST-1518291, HST-AR-14282, and HST-AR-13888. Additionally, I would like to acknowledge the computational resources of the Texas Advanced Computing Center (TACC), the NASA Advanced Supercomputing (NAS) Division and the NASA Center for Climate Simulation (NCCS), and the Extreme Science and Engineering Discovery Environment (XSEDE), which is supported by National Science Foundation grant number OCI-1053575.

CURRICULUM VITAE

Tyler Evan Kelley

EDUCATION

Doctor of Philosophy in Physics **2019**
University of California, Irvine *Irvine, CA*

Master of Science in Physics **2016**
University of California, Irvine *Irvine, CA*

Bachelor of Science in Astronomy **2010**
University of Minnesota *Minneapolis, MN*

Bachelor of Science in Physics **2010**
University of Minnesota *Minneapolis, MN*

RESEARCH EXPERIENCE

Graduate Research Assistant **2015–2019**
University of California, Irvine *Irvine, CA*

Undergraduate Research Assistant **2012–2014**
University of Minnesota *Minneapolis, MN*

TEACHING EXPERIENCE

Teaching Assistant **2014–2016**
University of California, Irvine *Irvine, CA*

FIRST AUTHOR REFREREED PUBLICATIONS

Phat ELVIS: The inevitable effect of the Milky Ways disk on its dark matter subhaloes **2019**
MNRAS 487 4409

CONTRIBUTING AUTHOR REFEREED PUBLICATIONS

Not so lumpy after all: modelling the depletion of dark matter subhaloes by Milky Way-like galaxies **2017**
MNRAS 471 1709

Galactic outflows, star formation histories, and timescales in starburst dwarf galaxies from STARBIRDS **2018**
MNRAS 477 3164

How low does it go? Too few Galactic satellites with standard reionization quenching **2019**
MNRAS 488 4585

Do Halos that Form Early, Have High Concentration, Are Part of a Pair, or Contain a Central Galaxy Potential Host More Pronounced Planes of Satellite Galaxies? **2019**
ApJ 875 105

ABSTRACT OF THE DISSERTATION

Phat ELVIS: The Inevitable Effect of the Milky Way's Disk

By

Tyler Evan Kelley

Doctor of Philosophy in Physics

University of California, Irvine, 2019

Professor James S. Bullock, Chair

We introduce an extension of the ELVIS project to account for the effects of the Milky Way galaxy on its subhalo population. Our simulation suite, Phat ELVIS, consists of twelve high-resolution cosmological dark matter-only (DMO) zoom simulations of Milky Way-size ΛCDM haloes ($M_{\rm v} = 0.7 - 2 \times 10^{12}$ M$_\odot$) along with twelve re-runs with embedded galaxy potentials grown to match the observed Milky Way disc and bulge today. The central galaxy potential destroys subhalos on orbits with small pericentres in every halo, regardless of the ratio of galaxy mass to halo mass. This has several important implications. 1) Most of the `Disc` runs have no subhaloes larger than $V_{\rm max} = 4.5$ km s^{-1} within 20 kpc and a significant lack of substructure going back ~ 8 Gyr, suggesting that local stream-heating signals from dark substructure will be rare. 2) The pericentre distributions of Milky Way satellites derived from *Gaia* data are remarkably similar to the pericentre distributions of subhaloes in the `Disc` runs, while the DMO runs drastically over-predict galaxies with pericentres smaller than 20 kpc. 3) The enhanced destruction produces a tension opposite to that of the classic 'missing satellites' problem: in order to account for ultra-faint galaxies known within 30 kpc of the Galaxy, we must populate haloes with $V_{\rm peak} \simeq 7$ km s^{-1} ($M \simeq 3 \times 10^7$ M$_\odot$ at infall), well below the atomic cooling limit of $V_{\rm peak} \simeq 16$ km s^{-1} ($M \simeq 5 \times 10^8$ M$_\odot$ at infall). 4) If such tiny haloes do host ultra-faint dwarfs, this implies the existence of ~ 1000 satellite galaxies within 300 kpc of the Milky Way.

Chapter 1

Introduction

A key prediction of standard ΛCDM cosmology is that dark matter (DM) haloes form hierarchically. This leads to the prediction that massive DM haloes receive a continuous influx of smaller haloes as they grow. Satellite galaxies have been detected around many galaxies and clusters, including the Milky Way (MW), and these are usually associated with the most massive subhaloes predicted to exist. As ΛCDM cosmological simulations have progressed to higher resolution, it has become clear that the mass spectrum of substructure rises steadily towards the lowest masses resolved (e.g. Springel et al., 2008; Kuhlen et al., 2009; Stadel et al., 2009; Garrison-Kimmel et al., 2014; Griffen et al., 2016). Testing this fundamental prediction stands as a key goal in modern cosmology. The present paper aims to refine existing predictions by including the inevitable dynamical effect associated with the existence of galaxies at the centers of galaxy-size dark matter haloes.

The 'missing satellites' problem (Klypin et al., 1999; Moore et al., 1999) points out a clear mismatch between the relatively small number of observed MW satellites and the thousands of predicted subhaloes above the resolution limit of numerical simulations. This discrepancy can be understood without changing the cosmology by assuming that reionization suppresses

star formation in the early Universe (Bullock et al., 2000; Somerville, 2002). Such a solution matches satellite abundances once one accounts for observational incompleteness (Tollerud et al., 2008; Hargis et al., 2014). As usually applied, these solutions suggests that haloes smaller than $\sim 5 \times 10^8\,\mathrm{M}_\odot$ ($V_{\mathrm{max}} < 15\ \mathrm{km\,s^{-1}}$, where V_{max} is defined as the maximum circular velocity) should be dark (Thoul & Weinberg, 1996; Okamoto et al., 2008; Ocvirk et al., 2016; Fitts et al., 2017; Graus et al., 2018a).

Detecting tiny, dark subhaloes would provide confirmation of a key prediction of ΛCDM theory and rule out many of the alternative DM and inflationary models that predict a cut-off in the power spectrum at low masses (Kamionkowski & Liddle, 2000; Bode et al., 2001; Zentner & Bullock, 2003; Horiuchi et al., 2016; Bozek et al., 2016; Bose et al., 2016). Since these haloes are believed to be devoid of baryons, they must be discovered indirectly. Within the Milky Way, one promising method for detecting dark subhaloes is via their dynamical effect on thin stellar streams, such as Palomar-5 and GD-1, which exist within ~ 20 kpc of the Galactic center (e.g. Johnston et al., 2002; Koposov et al., 2010; Carlberg et al., 2012; Ngan et al., 2015; Bovy et al., 2017; Bonaca et al., 2018, and references therein). With future surveys like LSST on the horizon, the number of detected streams around the MW should increase and hold information on the nature of dark substructure.

A statistical sample of MW-like haloes simulated in ΛCDM with sufficient resolution is necessary to make predictions for these observations. While several such simulations exist in the literature (e.g. Springel et al., 2008; Kuhlen et al., 2009; Stadel et al., 2009; Mao et al., 2015; Griffen et al., 2016), the vast majority are dark matter only (DMO). The use of DMO simulations to make predictions about subhalo properties is problematic because DMO simulations do not include the destructive effects of the central galaxy (D'Onghia et al., 2010). Hydrodynamic simulations show significant differences in subhalo populations compared to those observed in DMO simulations (Brooks & Zolotov, 2014; Wetzel et al., 2016; Zhu et al., 2016; Sawala et al., 2013, 2015). This is particularly true in the central regions of galaxy

haloes, where subhaloes are depleted significantly in hydrodynamic simulations compared to DMO counterparts (Garrison-Kimmel et al., 2017b; Despali & Vegetti, 2017; Graus et al., 2018b).

Garrison-Kimmel et al. (2017b) used the high-resolution hydrodynamic 'Latte' simulations (Wetzel et al., 2016) to show explicitly that it is the destructive effects of the central galaxy potential, not feedback, that drives most of the differences in subhalo counts between DMO and full-physics simulations. Their analysis relied on three cosmological simulations of the same halo: 1) a full FIRE-2 physics simulations, 2) a DMO simulation, and 3) a DMO simulation with an embedded galactic potential grown to match the central galaxy formed in the hydrodynamic simulation. They showed that most of the subhalo properties seen in the full physics simulation were reproduced in the DMO plus potential runs at a fraction of the CPU cost.

In this work, we expand upon the methods of Garrison-Kimmel et al. (2017b, GK17 hereafter) to make predictions for the dark substructure populations of the Milky Way down to the smallest mass scales of relevance for current dark substructure searches ($V_{\rm max} \simeq 4.5\ {\rm km\,s^{-1}}$). Unlike the systems examined in GK17, our central galaxies are designed to match the real Milky Way disk and bulge potential precisely at $z = 0$ and are grown with time to conform to observational constraints on galaxy evolution. Using 12 zoom simulations of Milky Way size haloes, we show that the existence of the central galaxy reduces subhalo counts to near zero within ~ 20 kpc of the halo center, regardless of the host halo mass or formation history. This suppression tends to affect subhaloes with early infall times and small pericenters the most. The changes are non-trivial and will have important implications for many areas that have previously been explored with DMO simulations. Some of these include the implied stellar-mass vs. halo-mass relation for small galaxies (Graus et al., 2018a; Jethwa et al., 2018), quenching timescales (Rodriguez Wimberly et al., 2018), ultra-faint galaxy completeness correction estimates (Kim et al., 2017), cold stellar stream heating rates (Ngan et al., 2015),

predicted satellite galaxy orbits (Riley et al., 2018), and stellar halo formation (Bullock & Johnston, 2005; Cooper et al., 2010). In order to facilitate science of this kind, we will make our data public upon publication of this paper as part of the ELVIS (Garrison-Kimmel et al., 2014) project site [1].

In section 2.1, we discuss the simulations and summarize our method of inserting an embedded potential into the center of the host; section 2.2 explores subhalo population statistics with and without a forming galaxy and presents trends with radius in subhalo depletion. We discuss further implications of our results in section 2.3 and conclude in section 2.4.

[1] `http://localgroup.ps.uci.edu/phat-elvis/`

Chapter 2

Phat ELVIS: The inevitable effect of the Milky Way's disk on its dark matter subhaloes

2.1 Simulations

All of our simulations are cosmological and employ the 'zoom-in' technique (Katz & White, 1993; Oñorbe et al., 2014) to achieve high force and mass resolution. We adopt the cosmology ofPlanck Collaboration et al. (2016, $\Omega_\Lambda = 0.6879$, $\Omega_\mathrm{m} = 0.3121$, $h = 0.6751$). Each simulation was performed within a global cosmological box of length $50\,h^{-1}\,\mathrm{Mpc} = 74.06$ Mpc. We chose each high-resolution region to contain a single MW-mass ($\sim 10^{12}\,\mathrm{M}_\odot$) halo at $z = 0$ that has no neighboring haloes of similar or greater mass within 3 Mpc. We focus on twelve such haloes, spanning the range of halo mass estimates of the MW summarized in Bland-Hawthorn & Gerhard (2016): $M_\mathrm{v} = 0.7 - 2 \times 10^{12}\,\mathrm{M}_\odot$. Haloes were selected based only on their virial mass with no preference on merger history or to the subhalo population. The

Component	Mass ($10^{10}\,\mathrm{M}_\odot$)	Scale Radius (kpc)	Scale Height (kpc)
Stellar Disk	4.1	2.5	0.35
Gas Disk	1.9	7.0	0.08
Bulge	0.9	0.5	—

Table 2.1: Parameters for the Milky Way potential components at $z = 0$ used in every `Disk` run. The disk scale radii correspond to exponential disk radii, which we model analytically by summing three Miyamoto & Nagai (1975) disk potentials following Smith et al. (2015). The buldge radius corresponds to the scale radius of a Hernquist (1990) potential. Parameters were taken from McMillan (2017) and Bland-Hawthorn & Gerhard (2016).

high-resolution regions have dark matter particle mass of $m_{\mathrm{dm}} = 3 \times 10^4\,\mathrm{M}_\odot$ and a Plummer equivalent force softening length of 37 pc. This allows us to model and identify subhaloes conservatively down to maximum circular velocity $V_{\mathrm{max}} > 4.5\ \mathrm{km\,s^{-1}}$, which corresponds to a total bound mass $M \gtrsim 5 \times 10^6\,\mathrm{M}_\odot$.

We ran all simulations using `GIZMO` (Hopkins, 2015)[1], which uses an updated version of the TREE+PM gravity solver included in `GADGET-3` (Springel, 2005). We generated initial conditions for the simulations at $z = 125$ using `MUSIC` (Hahn & Abel, 2011) with second-order Lagrangian perturbation theory. We identify halo centers and create halo catalogs with `Rockstar` (Behroozi et al., 2013a) and build merger trees using `consistent-trees` (Behroozi et al., 2013b) based on 152 snapshots spaced evenly in scale factor. The merger trees and catalogs allow us to identify basic halo properties at each snapshot, including the maximum circular velocity V_{max} and virial mass M_{v} for the main progenitor of each host halo and subhalo. For each subhalo, we record the time it first fell into the virial radius of its host and also the largest value of V_{max} it ever had over its history, V_{peak}. In most cases V_{peak} occurs just prior to first infall.

For the embedded disk galaxy simulations, we insert the galaxy potentials at $z = 3$ ($t_{\mathrm{lookback}} \sim$ 11.7 Gyr), when galaxy masses are small compared to the main progenitor (typically, $M_{\mathrm{gal}}/$

[1] `http://www.tapir.caltech.edu/~phopkins/Site/GIZMO.html`

Simulation	$M_{\rm v}$ ($10^{12}\,{\rm M}_\odot$)	$R_{\rm v}$ (kpc)	$V_{\rm max}$ (km s^{-1})	$V_{\rm v}$ (km s^{-1})	$N_{\rm sub}$ < 25 kpc	$N_{\rm sub}$ < 50 kpc	$N_{\rm sub}$ < 100 kpc	$N_{\rm sub}$ < 300 kpc	$c_{\rm NFW}$	$z_{0.5}$
Hound Dog	1.95	330	192	160	118	551	1858	6212	10.02	1.14
Hound Dog `Disk`	1.95	330	202	160	12	213	925	4351	11.82	1.31
Blue Suede	1.74	317	196	154	48	304	1139	4368	12.36	0.74
Blue Suede `Disk`	1.76	319	206	155	4	106	678	3082	14.23	0.76
Teddy Bear	1.57	307	183	149	62	411	1562	5138	10.43	0.99
Teddy Bear `Disk`	1.58	307	196	149	4	130	817	3668	11.78	1.05
Las Vegas	1.35	292	175	142	65	336	1237	4200	11.21	0.83
Las Vegas `Disk`	1.40	295	189	143	8	104	644	2992	13.48	0.86
Jailhouse	1.17	278	170	135	71	283	965	3384	11.73	1.15
Jailhouse `Disk`	1.20	280	188	136	13	104	486	2555	15.58	1.21
Suspicious	1.08	271	158	131	60	339	1156	3520	9.58	0.96
Suspicious `Disk`	1.10	272	166	132	10	133	666	2639	11.23	0.97
Kentucky	1.09	271	183	132	75	298	899	2791	18.03	1.78
Kentucky `Disk`	1.08	271	202	131	9	85	365	1761	24.15	2.22
Lonesome	1.02	265	159	129	91	378	1154	3390	11.14	1.56
Lonesome `Disk`	1.04	267	180	130	5	121	494	2164	16.54	1.55
Tender	0.95	259	152	126	74	344	1070	3190	10.16	0.81
Tender `Disk`	0.96	260	171	126	7	97	448	2112	16.05	0.84
Hard Headed	0.85	250	160	121	97	492	1389	3296	14.54	1.79
Hard Headed `Disk`	0.89	253	179	123	14	175	782	2412	18.65	1.76
Shook Up	0.72	236	147	115	92	346	1007	2740	12.16	1.46
Shook Up `Disk`	0.73	238	173	115	8	138	561	1767	20.67	1.51
All Right	0.65	229	140	111	66	328	898	2544	12.02	1.69
All Right `Disk`	0.71	235	164	114	5	116	479	1765	17.10	1.28

Table 2.2: Discography of halo properties at $z = 0$. Haloes are listed in pairs corresponding to DMO (first) and those run with embedded galactic potentials (second, designated '`Disk`'). The remaining columns list the Bryan & Norman (1998) virial mass, virial radius, maximum circular velocity, $V_{\rm max}$, and virial velocity ($\sqrt{GM_{\rm v}/R_{\rm v}}$), along with the the total number of subhaloes with $V_{\rm max} > 4.5{\rm km\,s^{-1}}$ that survive to $z = 0$ within 25, 50, 100, and 300 kpc of the halo center, the concentration based off of a best fit NFW, and the redshift at which the host obtained 50% of its final mass.

$M_{\rm v}\,(z=3) \simeq 0.03$). Prior to $z=3$, the `Disk` runs and DMO simulations are identical. At $z=3$, we impose the galaxy potential, which is centered on a sink particle with softening length 0.5 kpc and mass $10^8\,{\rm M}_\odot$. The sink particle is initially placed in the center of the host halo, as determined by `Rockstar`. We have found that dynamical friction keeps the sink particle (and thus the galaxy potential) centered on the host halo throughout simulations – with a maximum deviation from center of ~ 150 pc at $z=0$. Host halo mass accretion rates, positions, and global evolution are almost indistinguishable from the DMO runs after the galaxy potentials are included. As discussed below, the galaxy potential grows with time in a way that tracks dark matter halo growth. All galaxy potentials at $z=0$ are the same, with properties that match the Milky Way today, as summarized in Table 2.1. This means that our higher $M_{\rm v}$ halos will have smaller $M_{\rm gal}/M_{\rm v}$ ratios, where $M_{\rm gal} = M_{\rm stellar\,disk} + M_{\rm gas\,disk} + M_{\rm bulge}$. The full range of our suite it $M_{\rm gal}/M_{\rm v} \simeq 0.035 - 0.1$.

The properties of our twelve pairs of host haloes, along with the number of resolved subhaloes identified by `Rockstar` within several radial cuts of that host, are listed in Table 2.2. The first column lists the name of each simulated halo. The names are inspired by the twelve greatest[2] songs recorded by the Elvis Presely over his 24 year musical career. Haloes are listed in DMO/disk-run pairs, such that the disk simulations are identified with an added '`Disk`' to the name. Virial masses and radii (columns 2 and 3) use the Bryan & Norman (1998) definition of virial mass. Columns 4 and 5 list $V_{\rm max}$ and virial velocity, $V_{\rm v}$. Columns 6-9 give the cumulative count of subhaloes with $V_{\rm max} > 4.5\ {\rm km\,s^{-1}}$ within 25, 50, 100, and 300 kpc of each host's center. As we discuss below, the difference in subhalo counts between the `Disk` runs and DMO runs is systematic and significant, especially at small radii. Column 10 lists the best-fit Navarro et al. (1997, NFW) concentration for each halo. Note that the `Disk` runs are always more concentrated, even though their formation times (column 11) are similar. This particularly true of the lower mass host halos. The reason is that the dark matter in the host haloes contract in response to the central galaxy.

[2]As determined scientifically using Bayesian statistics and ideas motivated by string theory.

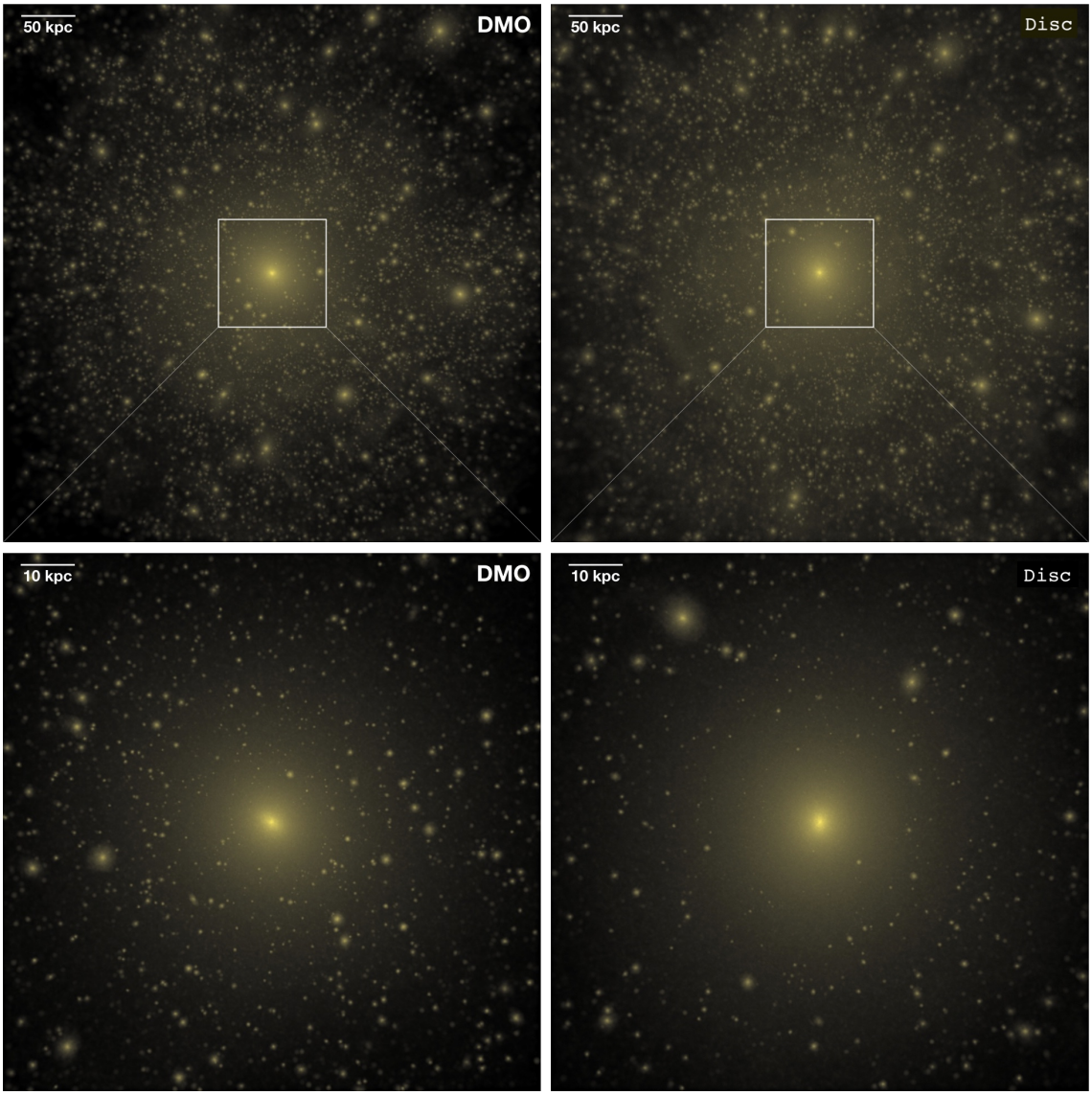

Figure 2.1: Visualization of the dark matter for Kentucky (left) and Kentucky `Disk` (right). The top panels span 500 kpc, approximately the virial volume of this halo. The bottom panels span 100 kpc. The absence of substructure at small radii in the `Disk` runs is striking. An enhancement in central dark matter density is also seen in the `Disk` runs, which is a result of baryonic contraction. The disk potentials are oriented face-on in these images.

Throughout this work we characterize subhaloes in terms of their $V_{\rm max}$ and $V_{\rm peak}$ (peak $V_{\rm max}$). We do this because we have found $V_{\rm max}$ selection to produce more consistent results between halo finders (e.g. `Rockstar` and `AHF`) than mass selection (for subhaloes in particular, mass definitions are more subjective). For reference, Garrison-Kimmel et al. (2014) found median relations between velocity and mass of $M_{\rm peak}/M_\odot \simeq 9.8 \times 10^7 (V_{\rm peak}/10\ {\rm km\,s^{-1}})^{3.33}$ and $M/M_\odot \simeq 9.1 \times 10^7 (V_{\rm max}/10\ {\rm km\,s^{-1}})^{3.45}$.

2.1.1 Embedded Potentials

The effects of the central baryonic disk is included in the DMO simulations following the basic technique described in Garrison-Kimmel et al. (2017b). Our embedded potentials are more detailed than those used by GK17 in order to more accurately model the MW galaxy. Specifically, we include an exponential stellar disk, an exponential gaseous disk, and a Hernquist bulge component. The galaxy potentials evolve from high redshift using empirically-motivated scaling relations (see 2.1.1) and we force them to match currently observed MW properties at $z = 0$. These $z = 0$ properties are taken from McMillan (2017) and Bland-Hawthorn & Gerhard (2016) as summarized in Table 2.1. For simplicity, we hold all disk orientations fixed throughout the simulation. The analysis in section 3.4 of GK17 suggests that the results do not largely depend on the orientation or shape of the embedded potential.

Modeling Evolution

We allow the galaxy potential to evolve with time by letting it track the dark matter halo growth using abundance matching (AM, Behroozi et al., 2013c). We enforce a constant offset in stellar mass at fixed halo mass such that the $z = 0$ galaxy mass matches the desired MW stellar disk mass at $z = 0$ for each of the simulations. Note that each halo has a different

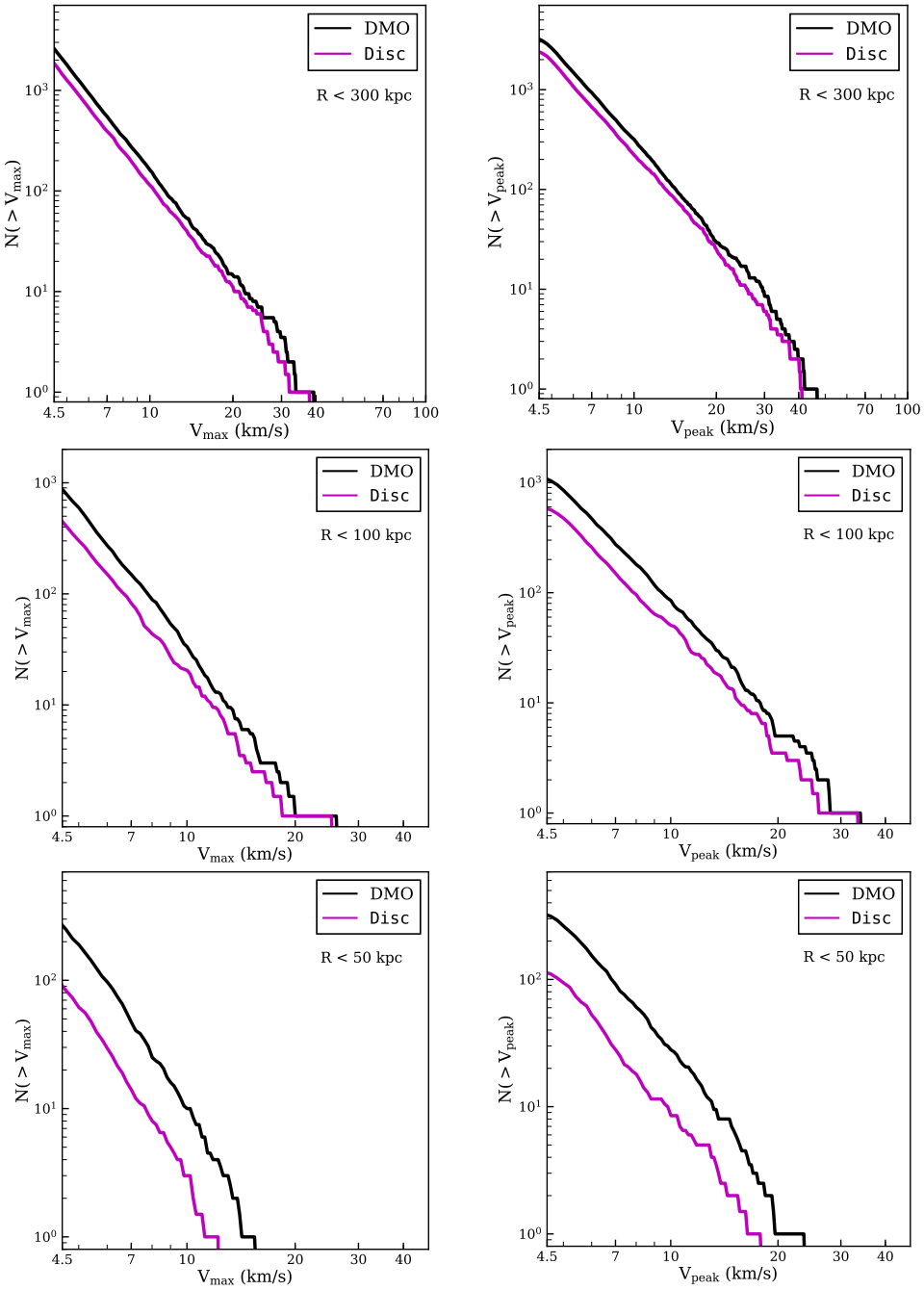

Figure 2.2: Cumulative $V_{\rm max}$ (left) and $V_{\rm peak}$ (right) distributions for subhaloes within $R =$ 300, 100, and 50 kpc (top to bottom) for all 12 of our DMO (black) and DMO+`Disk` runs (magenta). The solid lines are medians while the shaded bands span the full extent of the distributions. Note that the roll-off at low $V_{\rm peak}$ in the right panels are signatures of incompleteness. The $V_{\rm peak}$ completeness limit gets worse as we approach the halo centers (where stripping is more important). The simulations appear reasonably complete to $V_{\rm peak} \simeq$ 5km s^{-1} within 300 kpc. This limit drops to $V_{\rm peak} \simeq 6$ km s^{-1} within 50 kpc. There is no such roll-off in $V_{\rm max}$, which suggests we are complete down to $V_{\rm max} \simeq 4.5$ km s^{-1} throughout the haloes.

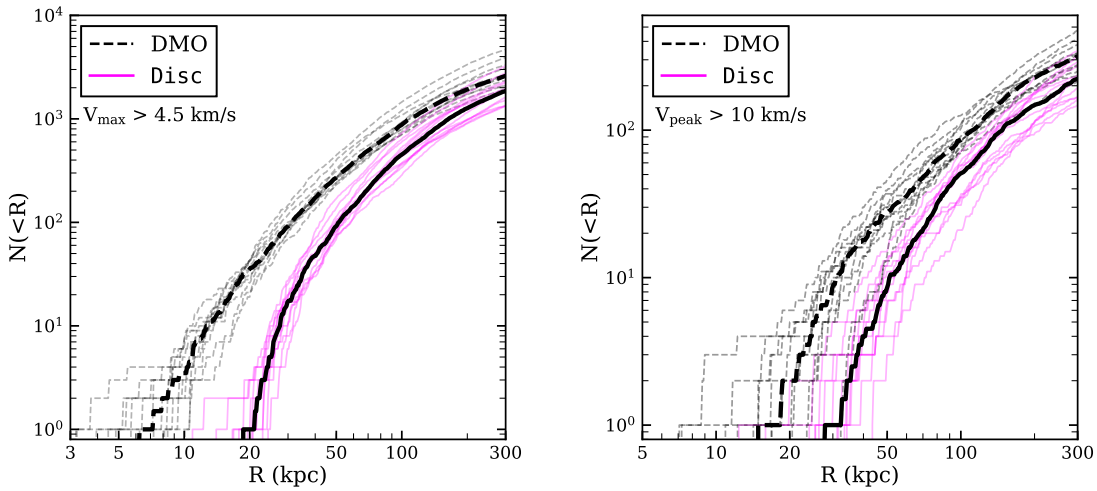

Figure 2.3: Cumulative counts for subhaloes within a given radius of the host. The black dashed lines represent the dark matter only runs and the magenta lines represent the same haloes with an embedded MW-like potential. Left: subhaloes with $V_{\rm max} > 4.5\,{\rm km\,s^{-1}}$. Right: subhaloes with $V_{\rm peak} > 10\,{\rm km\,s^{-1}}$. Note that the vertical axis scales are significantly different on the left and right.

$z = 0$ virial mass (Table 2.2) and this means that each one has a different offset from the mean AM relation throughout its history. If it is low at $z = 0$, it is low at $z = 3$ and vice versa. However, while each galaxy/halo has a distinct growth rate, all of them end up the same observationally-constrained 'Milky Way' galaxy at $z = 0$.

The scale radii at higher redshift are matched to median results from CANDELS, specifically those listed in Table 2 of van der Wel et al. (2014). The scale height is adjusted to keep the ratio between the scale length and height constant throughout time, with the $z = 0$ ratio as the chosen value. While this will keep the proportions of galaxy components constant, the overall size of the galaxy grows with time as informed by observations. The galaxy mass evolution for one of our hosts is shown in Figure 2.4 for reference.

Stellar Disk

The stellar disk of most galaxies is well represented with an exponential form (Freeman, 1970). However, the potential for such a distribution cannot be derived analytically. An alternative analytic potential commonly used is the Miyamoto & Nagai (1975, MN) disk potential:

$$\Phi(R, z) = \frac{GM_d}{\sqrt{R^2 + \left(R_d + \sqrt{z^2 + b^2}\right)^2}} \tag{2.1}$$

where M_d is the total disk mass, R_d is the scale length, b is the scale height, and R and z are the radial and vertical distances from the center, respectively.

Unfortunately, a single MN disk is a poor match to an exponential disk. The surface density in the center is too low and the surface density too high at large radii. A better approximation comes from the combination of three MN disk potentials (Smith et al., 2015). This technique matches an exponential disk within 2% out to 10 scale radii. We adopt the fits provided by Smith et al. (2015) and sum three MN disks together to model the exponential stellar disk with our chosen scale height and scale length.

Gas Disk

The gaseous disk is modeled as an exponential by implementing the same triple MN disk technique discussed above (Smith et al., 2015). The gas disk masses at high redshift are determined using the observational results of Popping et al. (2015) who provide gas fractions, $f_g = M_{\rm gas}/(M_{\rm gas} + M_\star)$, for galaxies as a function of stellar mass. Specifically, we use their median values for the cold gas fraction as a function of stellar mass and redshift to fit a 2-D regression. We then use this fit along with the stellar disk mass and redshift to set the cold gas mass. The scale lengths of the gas disk are fixed to be the same constant ratio with the

stellar disk given at $z = 0$.

Stellar Bulge

The bulge is modeled as a Hernquist (1990) potential where the scale length is a constant multiple of the stellar scale length as determined by both components' scale lengths at $z = 0$. The bulge mass evolves to maintain the same ratio of bulge mass to stellar mass present at $z = 0$.

Example of an Evolutionary Track

Figure 2.4 provides an example growth history for Kentucky in order to illustrate how our galaxy components are evolved. The dashed black line shows the main progenitor halo growth. The solid black line shows the growth of the full galaxy mass. The stellar disk (blue dashed), gas disk (red dotted), and bulge (green dash-dot) are forced to the values listed in Table 2.1 at $z = 0$. The stellar mass (disk plus bulge) is set to track the host halo growth using abundance matching. The gas disk masses at high redshift are determined using the observational results of Popping et al. (2015) who provide gas fractions for galaxies as a function of stellar mass.

2.2 Results

Figure 2.1 shows example visualizations of the dark matter distribution for a typical halo in our suite simulated without (left) and with (right) the galaxy potential. This is the halo identified as "Kentucky" and "Kentucky `Disk`" in Table 2.2. The top panels are 500 kpc boxes, and correspond approximately the virial volume of this halo (with $R_{\rm v} \simeq 270$ kpc).

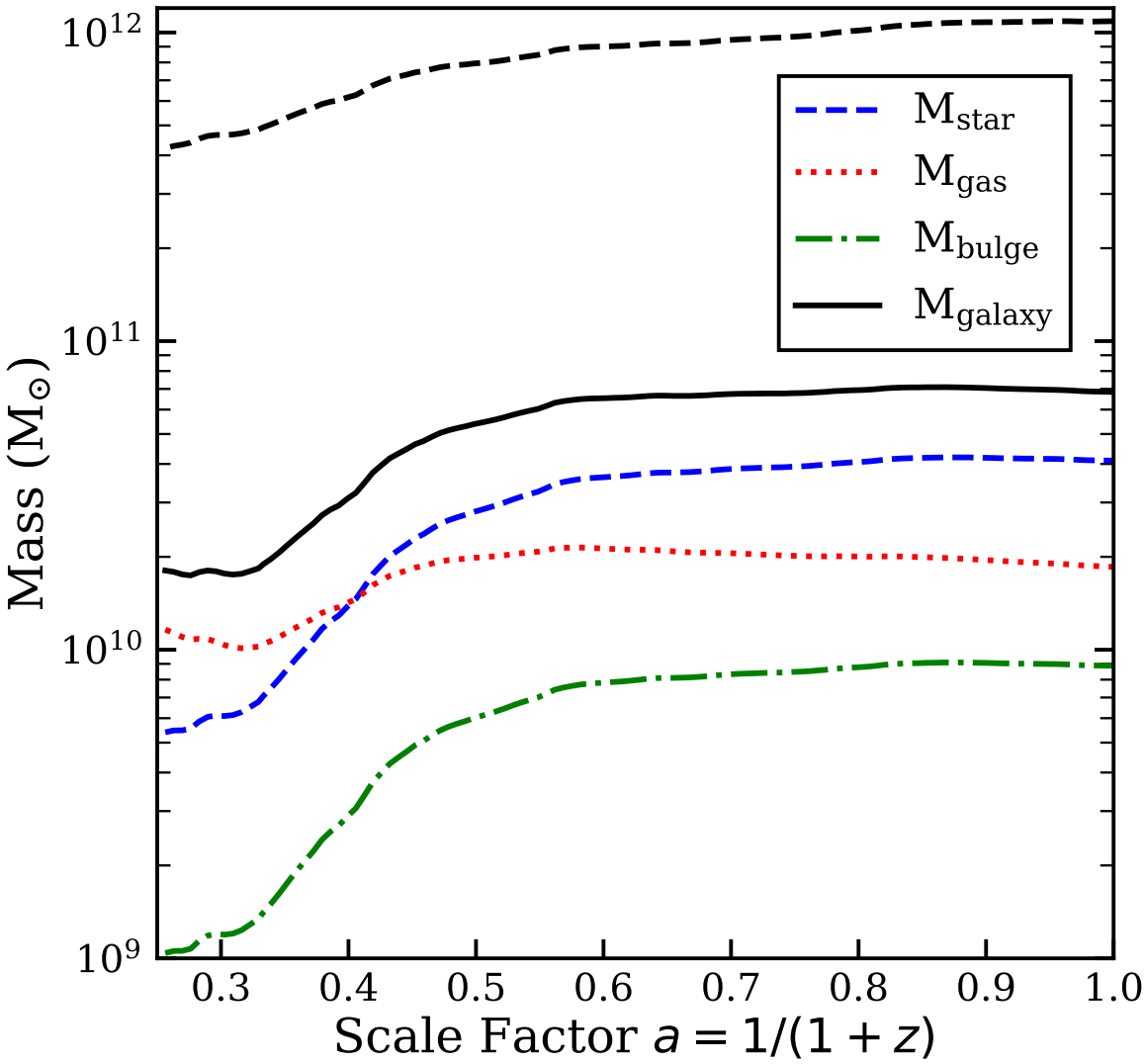

Figure 2.4: Mass growth of the galaxy for Kentucky with scale factor. The individual components' growths as well as the total galaxy mass growth. The final ($a = 1$) position of all galaxy lines (not the dark matter halo virial mass) is fixed for all hosts as discussed in section 2.1.1. The dashed line near the top of the figure shows the halo's virial mass evolution.

The lower panel is zoomed in to a region 100 kpc across. Qualitatively, our results are very similar to those of Garrison-Kimmel et al. (2017b). The presence of a central galaxy eliminates a majority of the substructure in the innermost region (≤ 50 kpc) but has only a minimal effect at large radius. The notable enhancement of dark matter the very center of the `Disk` run is due to baryonic contraction. This effect is also apparent in full hydrodynamic simulations at this mass scale (Garrison-Kimmel et al., 2017a).

2.2.1 Velocity Functions

Figure 2.2 shows the velocity functions for subhaloes in the DMO (black) and disk simulations (magenta). Shown are cumulative $\mathrm{V_{max}}$ distributions (left columns) and $\mathrm{V_{peak}}$ distributions (right column) of all the resolved subhaloes within 300 kpc, 100 kpc, and 50 kpc in top, middle, and bottom rows, respectively. The bands bound the minimum and maximum values for each velocity bin and the thick lines represent the medians. The inclusion of a central galaxy potential (magenta) to the DMO runs affects subhaloes of all masses roughly uniformly and has a greater impact on the total number of subhaloes in regions closer to the disk. Within 300 kpc, the `Disk` runs have $\sim 70\%$ the number of subhaloes seen in the DMO runs, roughly independent of velocity. At 100 kpc, the offset is close to a factor of ~ 2. Within 50 kpc, the difference is close to a factor of ~ 3.

One important feature seen in Figure 2.2 is the roll-off in the $V_{\rm peak}$ functions at small velocity. This is both a sign and measure of incompleteness. Incompleteness in $V_{\rm peak}$ gets worse at smaller radius (where stripping is more important) as might be expected. Within 100 kpc (middle right) we show signs of incompleteness below $V_{\rm peak} \simeq 5$ km s^{-1}. Within $R = 50$ kpc (bottom right) we appear complete for $V_{\rm peak} > 6$ km s^{-1}. Note that we show no major signs of completeness issues down to $V_{\rm max} = 4.5$ km s^{-1} for all radii we have explored. In Appendix 2.3.3 we present a resolution test using re-simulations of a DMO and `Disk` run

with 64 times worse mass resolution. Scaling from $V_{\rm max} = 4.5$ km s^{-1} to the lower resolution simulation, we would expect convergence down to $V_{\rm max} \simeq 15$ km s^{-1} (following the mass trend for subhalos, $M \propto V_{\rm max}^{3.45}$). We indeed find agreement with the higher resolution simulation at $V_{\rm max} = 15$ km s^{-1} in both the DMO and `Disk` resimulations.

2.2.2 Radial Distributions

As seen in Figure 2.2, the difference between the DMO and `Disk` runs increase with decreasing distance from the halo center. This point is emphasized in Figure 2.3, which shows cumulative radial profiles at fixed $V_{\rm max}$ (left) and $V_{\rm peak}$ (right) cuts in both DMO and `Disk` runs.

The left panel of Figure 2.3 shows the cumulative radial count of subhaloes with $V_{\rm max} >$ 4.5 km s^{-1} for each of our 12 DMO (black dash) and `Disk` (magenta) hosts. The thick black lines show medians for each of the distributions. Note that while the difference in overall count is only $\sim 30\%$ out at 300 kpc, the offset between DMO and `Disk` grows to more than an order of magnitude at small radius, and is typically a factor of ~ 20 at $R = 25$ kpc. The majority of the `Disk` runs have no identifiable substructure within 20 kpc. None of the `Disk` simulations have even a single subhalo within 10 kpc. As can be seen in Table 2.2, the systematic depletion of central subhaloes occurs in every host, including the most massive halo (Hound Dog), where the ratio of galaxy mass to halo mass is the smallest.

The right panel of Figure 2.3 tells a similar story. Here we have chosen a fairly large cut in $V_{\rm peak} > 10$ km s^{-1}. This scale is similar to, though somewhat smaller than, the natural scale where galaxy formation might naively be suppressed by an ionizing background (e.g. Okamoto et al., 2008). The majority of the `Disk` runs have nothing with $V_{\rm peak} > 10$ km s^{-1} within ~ 30 kpc. As discussed in Section 2.3.1 and in Graus et al. (2018a), the fact that we already know of 5 Milky Way satellites within 30 kpc of the Galactic center (and that we are not complete to ultra-faint galaxies over the full sky) suggests that we may need to

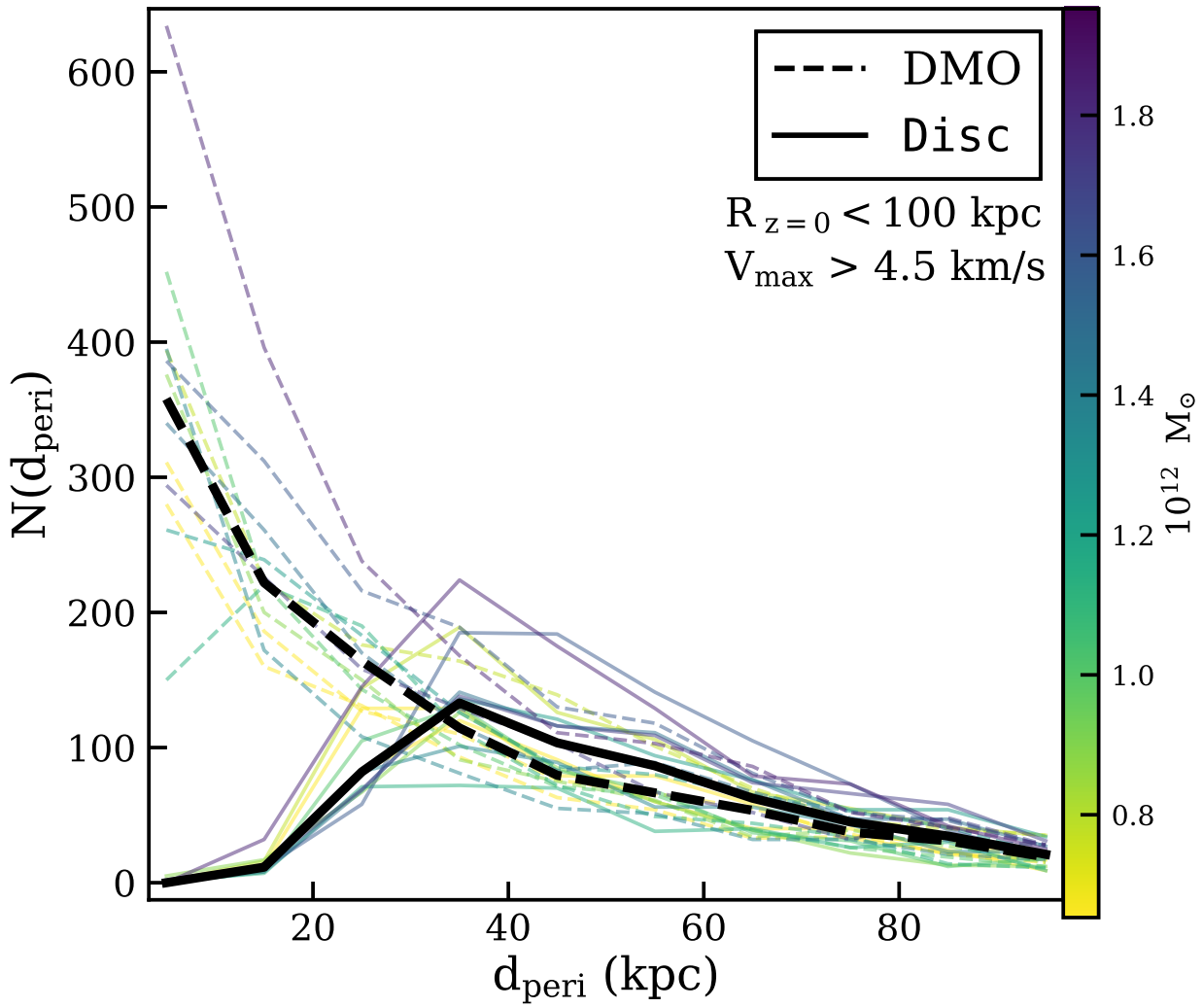

Figure 2.5: Distribution of the pericentric distances for all surviving subhaloes with $V_{\rm max} > 4.5\ {\rm km\,s^{-1}}$ within a present-day radius of $R = 100$ kpc. The dashed and solid lines represent the subhalo distributions for individual host haloes in DMO and `Disk` runs, respectively. The lines are colored according to host halo mass as indicated by the color bar on the right. We do this to provide a way to help match haloes from one run to the next, not because there is any apparent trend with halo mass. The thick lines show median relations for their respective simulation type. Note that the `Disk` runs preferentially deplete subhaloes that have pericenters smaller than $\sim 20 - 30$ kpc. While the DMO simulations have pericenter distributions that spike towards zero, subhaloes in the `Disk` runs have pericenter distributions that peak at ~ 35 kpc.

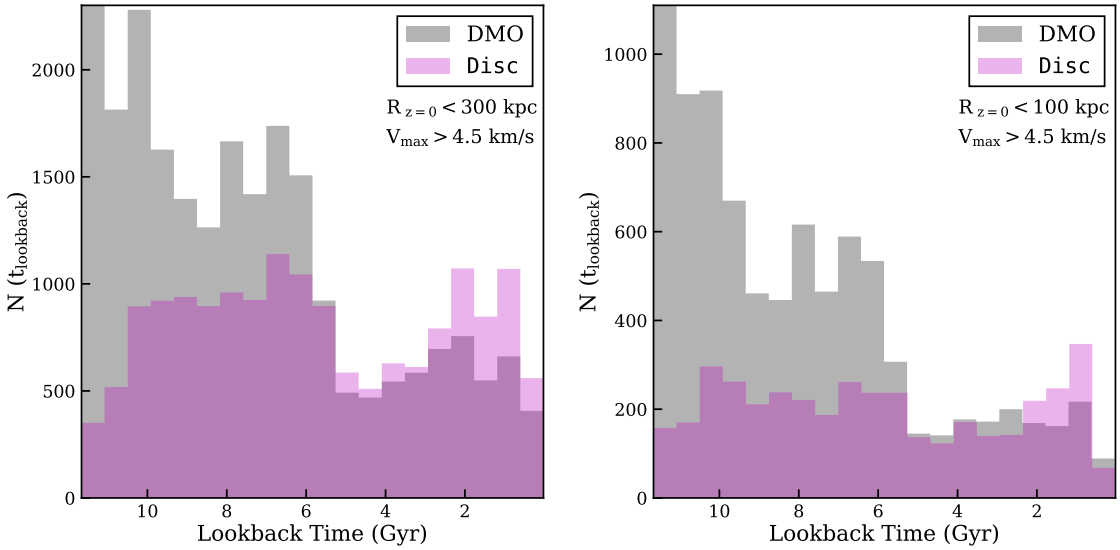

Figure 2.6: Distributions of infall times when subhaloes first crossed into the host virial radius. Shown are distributions for all surviving subhaloes with $V_{\rm max} > 4.5$ km s^{-1} within $R = 300$ kpc (left) and $R = 100$ kpc (right) stacked together for all of the DMO (gray) and `Disk` (magenta) simulations in our suite. The `Disk` runs are clearly depleted in subhaloes that fell in more than ~ 6 Gyr ago compared to the DMO runs, and especially so in the $R < 100$ kpc sample.

populate haloes well smaller than this 'natural' scale of galaxy formation in order to explain the satellite galaxy population.

2.2.3 Pericenter Distributions

At first glance, it is potentially surprising that the existence of a galaxy potential confined to the central regions of a halo can have such a dramatic effect on subhalo counts at distances out to ~ 100 kpc. As first discussed by Garrison-Kimmel et al. (2017b), the pericenter[3] distribution of subhaloes provides some insight into this question.

Figure 2.5 shows the pericenter distributions of all subhaloes found within $R = 100$ kpc at $z = 0$ in both the DMO (dashed) and `Disk` runs (solid). There is a unique (thin) line for

[3]Pericenters were obtained by interpolating the subhalo positions between snapshots and storing the minimum separation between the host and the subhalo as the pericenter. The time between interpolated snapshots is 14-16 Myr.

each halo, color coded by the halo virial mass (color bar). The thick black lines are medians. While the two distributions are similar for large pericenter differences ($R \gtrsim 40$ kpc) the differences are dramatic at $R \lesssim 20$ kpc. Subhaloes in the DMO simulations exist on quite radial orbits, with $d_{\rm peri}$ distributions that spike towards $d_{\rm peri} = 0$. Surviving subhaloes haloes in the `Disk` runs, on the other hand, have distributions that peak at $d_{\rm peri} \sim 35$ kpc and have a sharp decline towards $d_{\rm peri} = 0$. It is clear that subhaloes that get close to the galaxy potentials are getting destroyed.

Figure 2.5 also shows that the differential effect of the disk potential on a given halo varies dramatically based on the underlying orbital distribution of its subhaloes. DMO haloes that have the largest spike in low pericenters will have the largest overall shift in subhalo counts once disk potentials are included. We find that for subhaloes that exist within 300 kpc but have never passed within 20 kpc, the difference in the radial and orbital distributions between the DMO and `Disk` runs is negligible.

2.2.4 Infall Times

The subhaloes that are present in the DMO runs but absent in the `Disk` runs are biased not only in their orbital properties (Figure 2.5) but in the time they have spent orbiting within their host haloes. Figure 2.6 shows the infall time distributions for subhaloes with $V_{\rm max} > 4.5\ {\rm km\,s^{-1}}$ for all of the DMO simulations (gray) and for the `Disk` re-runs (magenta). The left panel shows infall times for subhaloes that exist within 300 kpc of their host halo centers at $z = 0$. The right panel shows infall times for subhaloes within 100 kpc. Times are plotted as lookback ages, with zero corresponding to the present day.

Both panels of Figure 2.6 clearly demonstrate that subhaloes with early infall times are preferentially depleted in the `Disk` runs. The differences are particularly significant for infall times greater than 6 Gyr ago: the early-infall tails are considerably depressed in the `Disk`.

Interestingly, the shifts in median lookback times to infall are modest as we go from DMO to `Disk`: 7.6 Gyr to 6.1 Gyr in the 300 kpc panel and 8 Gyr to 6 Gyr in the 100 kpc panel. Also, the `Disk` simulations show a slight *enhancement* of late-time accretions ($\sim 1-2$ Gyr). This may be related to the halo contraction that occurs as the galaxy grows at late times (see concentration comparison in Table 2.2). It is possible that some subhalos enter the viral volume faster than they would in the DMO equivalent because of this effect. More analysis will be needed to test this hypothesis because the halo virial mass itself shows no such enhancement at late times.

2.2.5 Time Evolution of Substructure Counts

Substructure in dark matter haloes is set by a competition between the accretion rate of small haloes and the mass loss rate from dynamical effects over time (e.g. Zentner & Bullock, 2003). A central galaxy potential increases the destruction rate, which depletes subhalo populations compared to DMO simulations.

One question is whether and to what extent differences in subhalo counts seen between DMO and `Disk` runs persists at earlier times. This may have important observational implications for substructure probes that are sensitive properties at early times. Cold stellar streams, for example, may have existed for multiple orbital times ($t_{\rm orb} \sim 500$ Myr). If the substructure population was significantly higher in the past then this could manifest itself in observables today.

Figure 2.7 explores this question by showing the count of $V_{\rm max} > 4.5\ {\rm km\,s^{-1}}$ subhaloes within a physical radius of 20 kpc of each halo center as a function of lookback time. The bands show the full distributions over all simulations, with gray corresponding to DMO and magenta corresponding to the `Disk` runs. Solid lines are medians. We see that the overall offset between DMO and `Disk` runs persists to lookback times of 8 Gyr, but that for times prior

to ~ 4 Gyr ago, the subhalo counts in the `Disk` runs begin to approach the DMO counts. In the median, the difference is 'only' a factor of ~ 3 eight billion years ago, compared to more than a factor of ~ 30 suppression at late times.

Overall, it appears that the expected suppression is quite significant in its implications for cold stellar stream heating. The median count of subhaloes in the `Disk` runs remains near zero over the past ~ 2 Gyr (compared to ~ 50 subhaloes in the DMO runs). This timescale is > 3 orbital times for a cold stream like Pal-5 at $R = 20$ kpc and $V_{\rm orb} \sim 200$ km s^{-1}. The median subhalo count in the `Disk` runs remains less than ten to lookback times of 4 Gyr. Cold streams that have persisted for more than 4 Gyr or extend out to ~ 50 kpc from the Galaxy may be required in order to provide robust probes of substructure, though a full exploration of this question will require work well beyond that presented in this introductory paper. We hope that the public release of our subhalo catalogs will facilitate efforts of this kind.

2.3 Implications

2.3.1 What haloes host ultra-faint galaxies?

As alluded to in Section 2.2.2, the absence of substructure within the vicinity of the central galaxy in the `Disk` runs may have important implications for our understanding of the mapping between galaxy haloes and stellar mass. In particular, the relatively large number of galaxies that are known to exist within ~ 50 kpc of the Galactic center provides important information about the lowest mass dark matter haloes that are capable of forming stars (Jethwa et al., 2018).

The majority of efforts to understand how the ionizing background suppresses galaxy for-

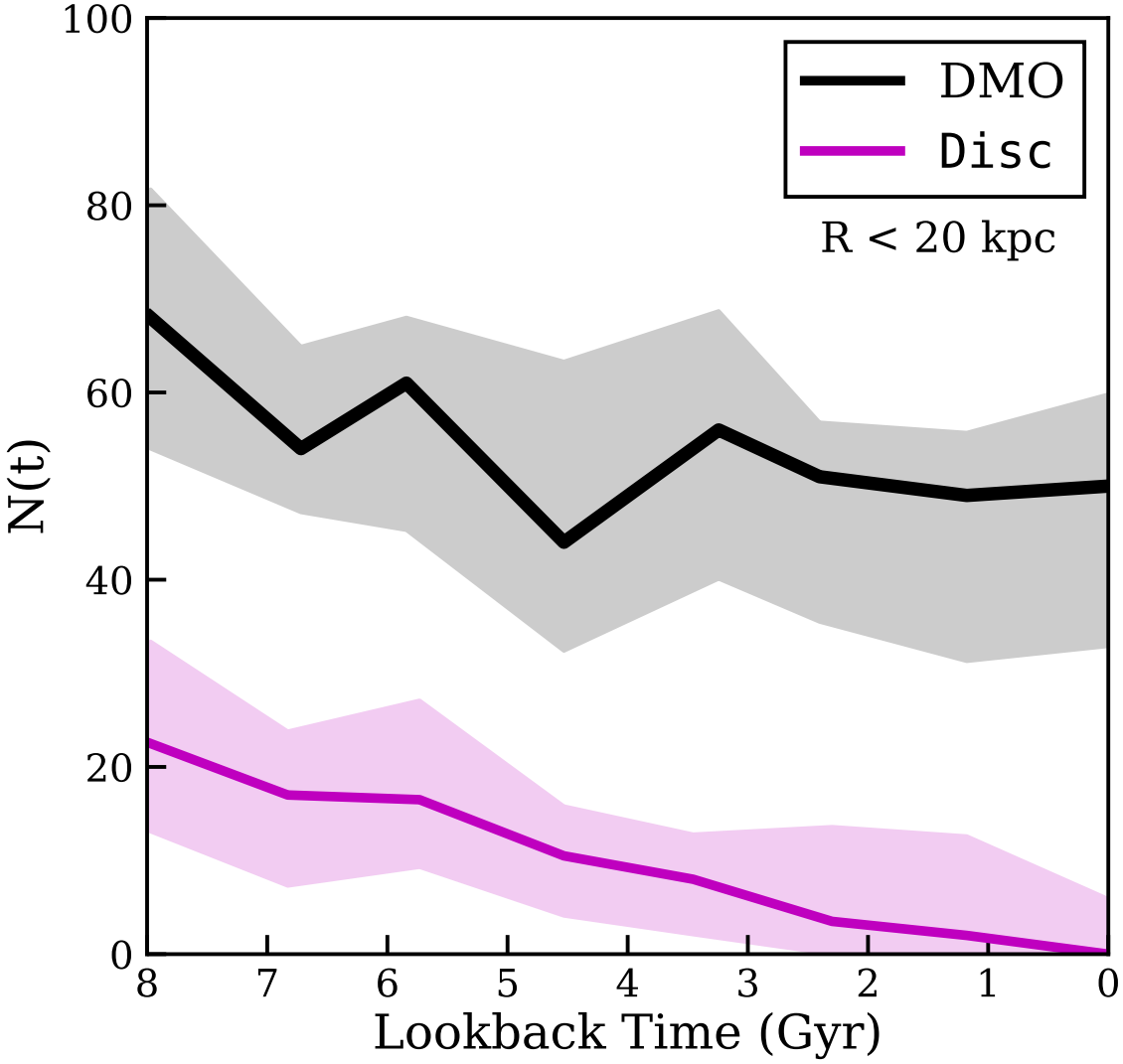

Figure 2.7: Number of subhaloes with $V_{\rm max} > 4.5$ km s^{-1} that exist within 20 kpc (physical) of the host halo center as a function of lookback time. The gray and magenta distributions represent the distributions for the DMO and `Disk` runs, respectively. The solid lines show medians and the bands cover the full spread of the data. The difference between the two classes of runs persists back to 8 Gyr.

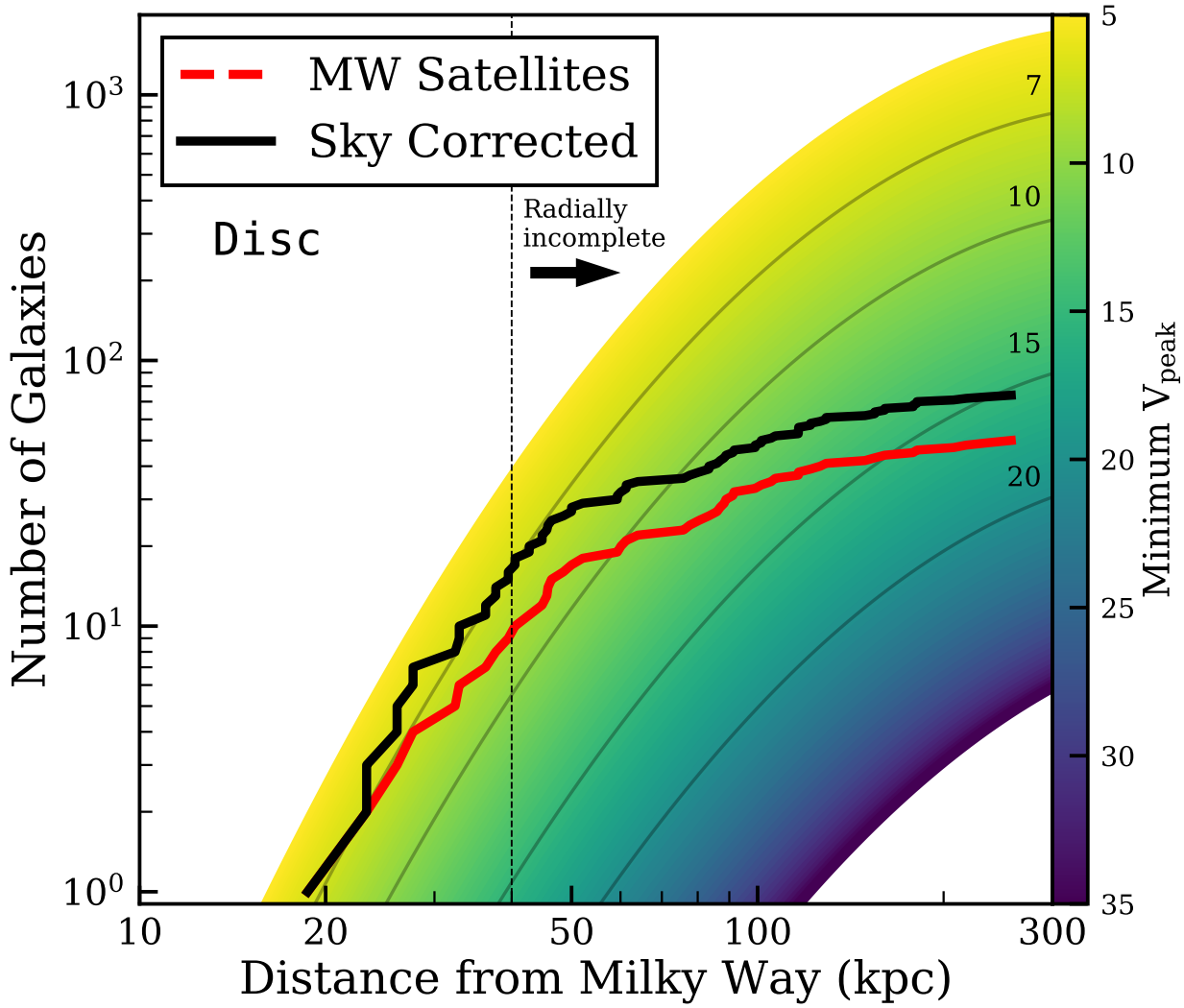

Figure 2.8: Median cumulative radial counts of subhalos for all of the `Disk` runs color coded by $V_{\rm peak}$ threshold. The faint gray lines mark $V_{\rm peak}$ thresholds larger than 7, 10, 15, and 20 km s^{-1}, respectively. Thick lines represent the Milky Way satellite data uncorrected (red dashed) and corrected for sky coverage (solid black). The vertical dotted line at 40 kpc represents an estimate of the radial completeness limit for $L \simeq 1000$ L$_\odot$ ultra-faint dwarfs. Observed counts to the right of this line should be treated as lower limits, as the true counts may be much higher than those shown given the lack of a deep, full sky survey. If our host halos are representative of the Milky Way, then we must populate all subhaloes with $V_{\rm peak} \gtrsim 7$ km s^{-1} in order to account for the data. This extrapolates to an implied total of ~ 1000 ultra-faint satellites within 300 kpc.

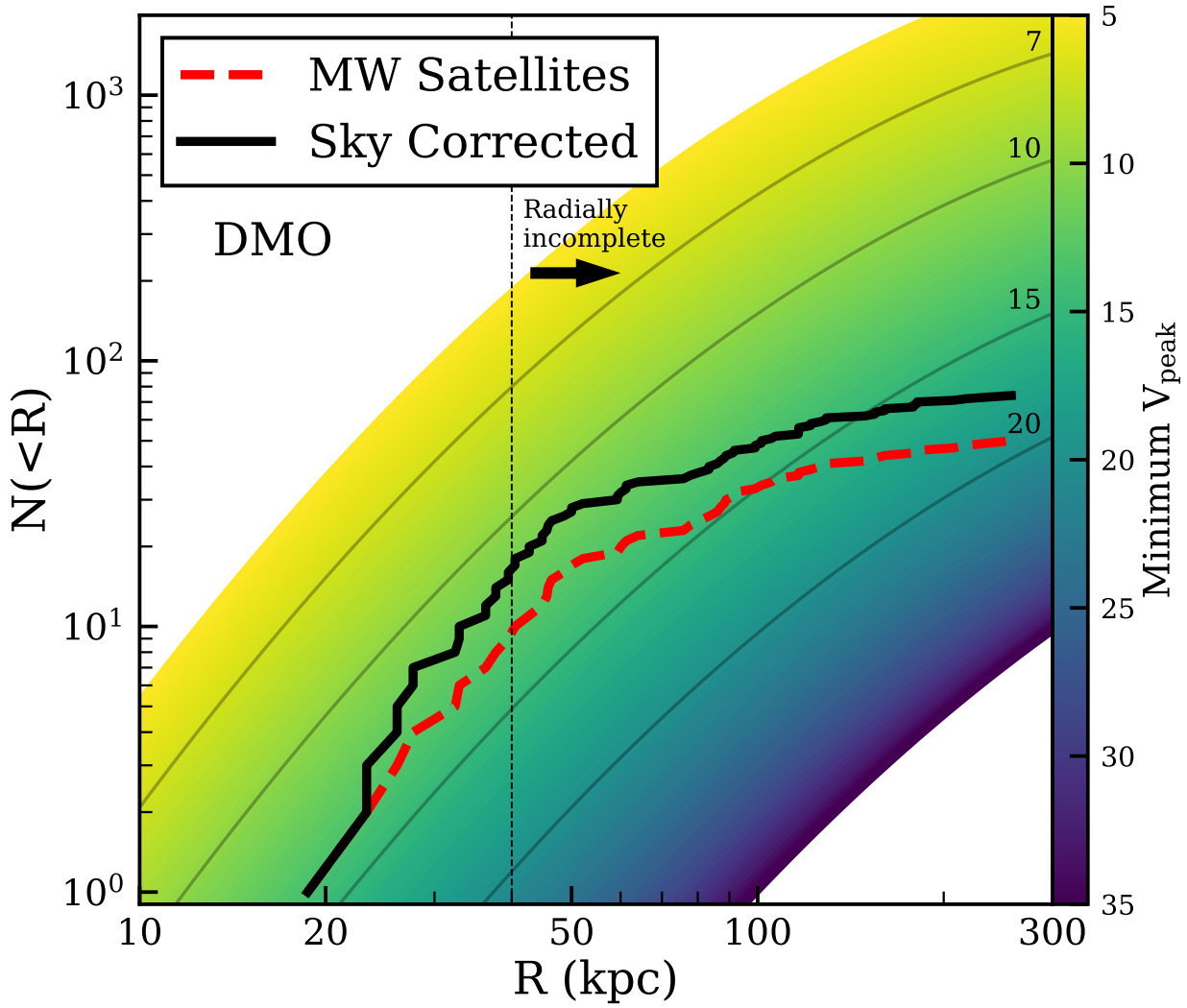

Figure 2.9: Median radial profiles for different $V_{\rm peak}$ cuts for all of the DMO runs. Compare to the `Disk` simulations shown in Figure 2.8. The faint gray lines represent the DMO data for fixed $V_{\rm peak}$ thresholds of 7, 10, 15, and 20 $\rm km\,s^{-1}$, respectively. The thick lines represent the Milky Way satellite data uncorrected (red dashed) and corrected for sky coverage (solid black). Haloes with $V_{\rm peak} \gtrsim 12$ $\rm km\,s^{-1}$ are required to match the inner data in the median of our DMO runs, and this extrapolates to an implied total of ~ 200 ultra-faint satellites within 300 kpc.

mation have found that most dark matter haloes with $V_{\rm peak} < 20$ km s^{-1} are devoid of stars (e.g., Thoul & Weinberg, 1996; Okamoto et al., 2008; Ocvirk et al., 2016; Fitts et al., 2017). A second scale of relevance for low-mass galaxy formation is the atomic hydrogen cooling limit at 10^4 K, which corresponds to a $V_{\rm peak} \simeq 16\,{\rm km\,s^{-1}}$ halo. Systems smaller than this would require molecular cooling to form stars. Taken together, one might expect that most ultra-faint satellite galaxies of the Milky Way should reside within subhaloes that fell in with peak circular velocities in the range $16 - 20\,{\rm km\,s^{-1}}$.

Compare this basic expectation to the information summarized in Figure 2.8. Here we plot the *median* cumulative radial count of subhaloes with $V_{\rm peak}$ values larger than a given threshold as derived from the full sample of `Disk` runs. The color bar on the right indicates the $V_{\rm peak}$ threshold and the solid lines track characteristic $V_{\rm peak}$ values (7, 10, 15, and 20 km s^{-1}) as labeled. A similar figure that utilizes data from the DMO simulations is provided in Figure 2.9.

The dashed red line shows the census [4] of known MW satellites galaxies as compiled by Fritz et al. (2018). The thick black line in Figure 2.8 applies a sky-coverage correction to derive a conservative estimate of the radial count of satellite galaxies. This correction assumes that 50% of the sky has been covered by digital sky surveys to the depth necessary to discover ultra-faint galaxies and adds a second galaxy for every MW dwarf known that has an absolute magnitude fainter than -6. Importantly, even in the region of the sky that has been covered by digital sky surveys like SDSS and DES, our census of the faintest ultra-faint galaxies ($L \lesssim 10^3$ L$_\odot$) is not complete at radii larger than ~ 40 kpc (Walsh et al., 2009). We draw attention to this fact with the vertical dotted line.

If our simulation suite is indicative of the Milky Way, we must associate the galaxies within 30 kpc with subhaloes that had maximum circular velocities at infall greater than just

[4] The Fritz et al. (2018) compilation does not include the LMC and SMC. We also exclude their presence here to be conservative, as massive subhalos of this kind are rare in MW-size hosts and we are focusing primarily on implications for ultra-faint satellites.

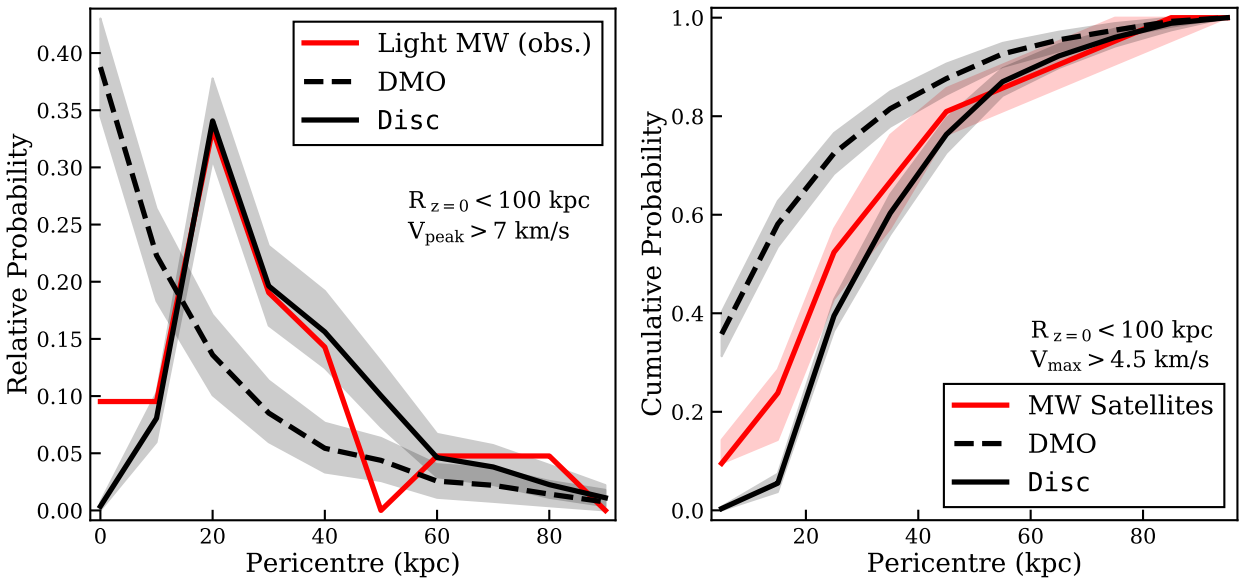

Figure 2.10: Comparison of the pericenter distributions for subhaloes (black) with $V_{\rm max} > 4.5$ km s^{-1} to those of the 21 MW satellites (red) within 100 kpc of the Galactic center as derived by Fritz et al. (2018). In order to account for radial completeness bias in the data, the subhaloes have been resampled to have the same $z = 0$ radial distribution as the data. Each host halo is weighted equally. Left: Differential DMO (dashed) and `Disk` (solid) median pericenter distributions with the MW satellite pericenter distribution shown in red. The gray bands represent the 95% confidence interval obtained from sampling the subhaloes pericenter distributions. Right: Cumulative pericenter distributions. The band represents the 95% confidence interval obtained from sampling the MW satellite pericenter values given their respective errors. Unlike the real MW satellites, the DMO subhaloes peak towards small pericenter. The `Disk` runs produce a subhalo pericenter distribution that is closer to the distribution seen in the data.

7 km s^{-1} (corresponding to a peak infall mass of $M_{\rm peak} \simeq 3\times10^7$ M$_\odot$, Garrison-Kimmel et al., 2014). This is not only well below the canonical photo-ionization suppression threshold ($\sim$ 20 km s^{-1}), it is smaller than the atomic cooling limit ($\sim$ 16 km s^{-1}). The virial temperature of the required $\sim$ 7 km s^{-1} haloes is 2000 K, which likely would need efficient molecular cooling for star formation to proceed. If we perform the same exercise host-by host, the minimum $V_{\rm peak}$ required to explain the galaxy counts within 40 kpc varies some. Nine of our 12 `Disk` runs require $V_{\rm peak} = 6.5-7.5$ km s^{-1} to explain the counts within 40 kpc. The other three require $V_{\rm peak} = 8.1$, 9.2, and 9.3 km s^{-1}, respectively. We find no trend between the minimum $V_{\rm peak}$ required to explain the known counts and host halo mass. In a companion paper by Graus et al. (2018a) we explore the implications of this basic finding and provide a statistical comparison based on each of our `Disk` runs individually.

In addition to changing our basic picture of low-mass galaxy formation, the need to populate tiny $V_{\rm peak} = 7$ km s^{-1} haloes with galaxies means that there should be a very large number of ultra-faint galaxies within the virial radius of the Milky Way. By tracking the 7 km s^{-1} line out to 300 kpc in Figure 2.8, we see that it reaches $\sim$ 1000 such objects. If they are there in such numbers, future surveys like LSST should find them. There would of course be many more outside of the virial radius. In the field, the number density of these tiny haloes is $\sim$ 100 Mpc^{-3} (e.g. Bullock & Boylan-Kolchin, 2017). This means that there may be 100,000 ultra-faint galaxies for every L_* galaxy in the universe.

Figure 2.9 is analogous to Figure 2.8 except now we compare the cumulative count of known MW galaxies to predictions for the DMO runs. There are many more haloes at small radii than in the `Disk` runs and this means that to account for the number of galaxies seen within $\sim$ 40 kpc we can populate more massive systems: $V_{\rm peak} \gtrsim 12$ km s^{-1} halos. If this were the case, we would expect only $\sim$ 200 ultra-faint galaxies to exist within 300 kpc of the Milky Way, which is in line with older expectations for satellite completeness limits based on DMO simulations (Tollerud et al., 2008). It is interesting that the slopes of the predicted

cumulative counts in Figure 2.8 are more similar to the observed radial profile of satellites within ~ 50 kpc than the profiles in the DMO runs shown in Figure 2.9. This is perhaps an indication that by including the existence of the Galactic disk, we are approaching a more accurate model of the Milky Way's satellite population.

2.3.2 Satellite Pericenters

As we discussed in reference to Figure 2.5, subhalo pericenter distributions are dramatically different once the galaxy potential is included. Here we take advantage of recent insights on satellite galaxy orbits made possible by *Gaia* to determine which of these distributions is more in line with observations (Gaia Collaboration et al., 2018; Simon, 2018; Erkal et al., 2018; Pace & Li, 2018; Fritz et al., 2018).

Figure 2.10 presents a comparison of subhalo pericenters in the DMO (dashed) and `Disk` runs (solid) to those of MW satellite galaxies. Shown in red are the differential (left) and cumulative (right) pericenter distributions of MW galaxies from Fritz et al. (2018) that have $z = 0$ distances within 100 kpc of the Galactic center. The Fritz et al. (2018) sample includes proper motions of 21 satellite galaxies within 100 kpc. Two MW potentials are used in Fritz et al. (2018) to derive the pericenter distances of each satellite. They are based on the *MWPotential14* potential (see Bovy 2015 for details) with a light and heavy DM halo with virial masses of $0.8 \times 10^{12}\,\mathrm{M}_\odot$ and $1.6 \times 10^{12}\,\mathrm{M}_\odot$, respectively. For clarity, we only include the results of the "Light" MW potential, which is closer to the median halo mass of our sample ($1.1 \times 10^{12}\,\mathrm{M}_\odot$). Results for the "Heavy" MW potential are very similar and can be found in Appendix 2.3.3.

In order to fairly compare predictions to observations in this space, we must account for observational incompleteness. Our current census of faint galaxies is radially biased within 100 kpc, such that we are missing galaxies at large radii. In order to make a fair comparison,

we took all subhaloes with $V_{\rm max} > 4.5$ km s^{-1} within a $z = 0$ distance of 100 kpc of the center of each halo and then subsampled those populations 1000 times for each halo to create present-day radial distributions that match those of the satellites in Fritz et al. (2018). We then "stacked" these populations together to derive median pericenter distributions for subhaloes in each of the two classes of simulations (DMO and `Disk`). Note that each host halo is equally weighted.

The left panel of Figure 2.10 compares the median of the radially re-sampled distributions to the distribution of pericenters derived by Fritz et al. (2018). As foreshadowed in Figure 2.5, the DMO subhaloes have a pericenter distribution that spikes towards small values, very unlike the distribution seen in the real data. The `Disk` runs, on the other hand, show a peak at ~ 30 kpc with rapid fall-off at smaller radii and a more gradually fall-off towards larger distances. This shape is quite similar to that seen in the real data. Note that if we choose subhaloes with $V_{\rm peak} > 7$ km s^{-1} instead, the distributions are almost indistinguishable (see Appendix 2.3.3). It is interesting that the total lack of subhaloes with pericenters smaller than 20 kpc is *not* seen in the data. The two galaxies in this inner bin are Segue 2 and Tucana III; these systems may very well be in the process of disruption.

In the right panel of Figure 2.10 we present the same data cumulatively and also explore how uncertainties in the derived orbits affect the comparison. Specifically, we used the quoted errors given by Fritz et al. (2018) on each galaxy and drew from a Gaussian to generate $10,000$ realizations for each system. The median of the resultant distribution is given by the thick red line with 95% confidence intervals shown by the shaded band. The DMO distribution is well above the 95% region everywhere within 50 kpc. The median of `Disk` runs remain within the spread for all but the inner most region.

From the above comparison, we conclude that the DMO runs produce a pericenter distribution for satellite subhaloes that is quite far from what is observed for Milky Way satellite galaxies. The `Disk` runs are much closer to what is observed and therefore appear to provide

a more realistic comparison set. The clear next step in this comparison is to re-derive the implied pericenter distributions for each host halo's mass and to directly compare predictions in full phase space to those observed. While such an analysis is beyond the scope of this introductory paper, future work in this direction is warranted. Understanding how host halo-to-halo scatter, ongoing satellite disruption, and specifics of halo finding affect these interpretations will also be important.

2.3.3 Effects of Different Models

Figure 2.11 is analogous to Figure 2.10 in that it compares the pericenter distributions of subhaloes to those of Milky Way satellite galaxies presented Fritz et al. (2018). Here we include the pericenters derived using both the "Light" (red) and "Heavy" (blue) MW potential in Fritz et al. (2018). We also show the subhalo distributions for a $V_{\rm max}$ cut ($> 4.5\ {\rm km\,s^{-1}}$, left) and $V_{\rm peak}$ cut ($> 7\ {\rm km\,s^{-1}}$, right). These different choices do not change the qualitative result that the observed satellite distributions are closer to the `Disk` runs than the DMO runs.

2.4 Discussion and Conclusions

In this paper, we have introduced Phat ELVIS suite of 12 high-resolution simulations of Milky Way mass dark matter haloes that are each run with (`Disk`) and without (DMO) a Milky Way disk galaxy potential. As summarized in Table 2, the host halo masses in our suite span $M_{\rm vir} = 0.7 - 2 \times 10^{12}\,{\rm M}_\odot$, which encompasses most recent estimates for the virial mass of the Milky Way (Bland-Hawthorn & Gerhard, 2016). The galaxy potential at $z = 0$ is the same for each `Disk` run and is summarized in Table 1. As demonstrated in Figure 2.2, our resolution allows us to have convergence in identifying subhaloes down to a maximum

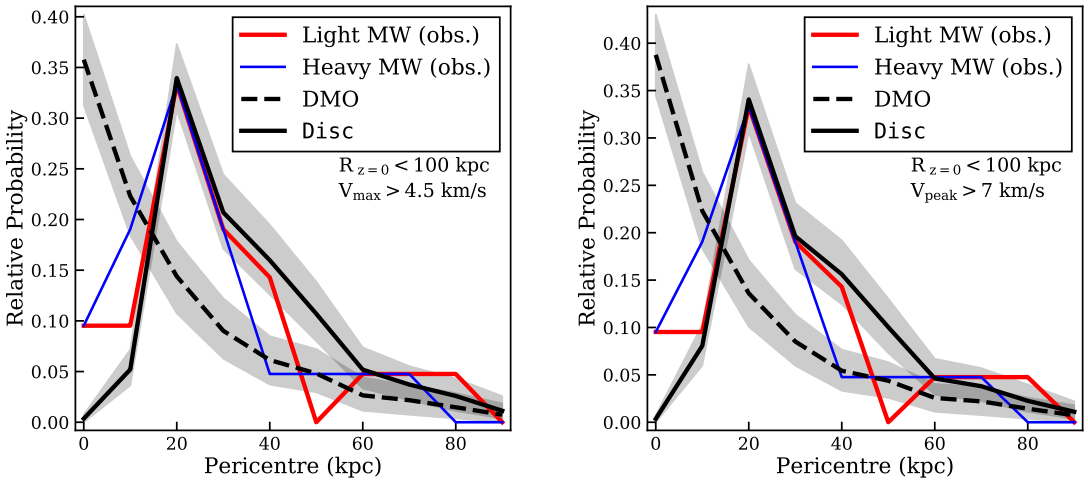

Figure 2.11: Differential pericenter distributions for subhaloes (black) with $V_{\rm max} > 4.5\,{\rm km\,s^{-1}}$ (left) and $V_{\rm peak} > 7\,{\rm km\,s^{-1}}$ (right) and MW satellites derived from both potentials used in Fritz et al. (2018). The pericenters derived using the "Light" MW potential are shown by the red line and is the same as figure 2.5 while those derived using the "Heavy" MW potential are shown by the blue line. The gray bands represent the 95% confidence interval for the subhaloes' distributions.

circular velocity of $V_{\rm max} = 4.5\,{\rm km\,s^{-1}}$ ($M \simeq 5 \times 10^6\,{\rm M_\odot}$) and with peak (infall) circular velocities $V_{\rm peak} \simeq 6\,{\rm km\,s^{-1}}$ ($M_{\rm peak} \simeq 1.8 \times 10^7\,{\rm M_\odot}$). The main effect of the Milky Way potential on subhalo populations is that subhaloes with pericenters smaller than ~ 20 kpc are depleted in the `Disk` runs (see Figure 2.5).

2.4.1 Impact of the Disk on substructure populations

The most striking difference between the `Disk` and DMO subhaloes is in their abundances at radii smaller than ~ 50 kpc at $z = 0$. This difference can be seen visually in Figure 2.1 and quantitatively in Figure 2.3. Table 2.2 lists counts as a function of various radial choices and shows that the ratio of subhalo counts between the `Disk` to DMO runs at $z = 0$ is typically $\sim 1/10$ at $R < 25$ kpc, $\sim 1/3$ at $R < 50$ kpc, and $\sim 1/2$ at $R < 100$ kpc. Note that these ratios are fairly constant independent of the host halo virial radius (or concentration). To

zeroth order, the depletion radius appears to be set by the disk potential (which is the same for all runs), not host halo properties. The most important predictor for relative depletion seems to be the variable pericenter distributions in the DMO runs: simulations that have subhaloes with an over-abundance of percienters smaller than ~ 20 kpc will experience more relative depletion once the galaxy potential is included.

Another difference between the surviving subhalo populations in the DMO and `Disk` runs is in the distribution of infall times (see Figure 2.6). If the galaxy potential is included, the majority of subhaloes that fell in more than ~ 8 Gyr ago and survived in the DMO runs become destroyed in the `Disk` runs. This may have important implications for models of environmental galaxy quenching when applied to the Milky Way (Rodriguez Wimberly et al., 2018; Fillingham et al., 2015; Wetzel et al., 2015; Wheeler et al., 2014) and may also potentially change the expected mapping between orbital energies and infall time expected for Milky Way satellites (Rocha et al., 2012).

2.4.2 Numerical Convergence

Before moving on to summarize some potential observational implications of our results, it is worth discussing numerical completeness. Figure 2.2 provides evidence that the mass functions are converged for subhaloes with infall masses down to $M_{\rm peak} \simeq 1.8 \times 10^7\,{\rm M}_\odot$ ($\rm N_p \sim 600$ particles). This level of completeness is typical of that quoted for simulations of this kind (e.g. Springel et al., 2008; Garrison-Kimmel et al., 2014). In Appendix 2.3.3 we present a resolution test using a re-simulation of one of our halos with 64 times worse mass resolution, and show that we are indeed converged to subhalos that are 64 times more massive than we have estimated in the high-resolution runs. We also show using this low-resolution comparison that there is not a significant difference in convergence between the DMO and `Disk` runs. This suggests that the offset between our `Disk` and DMO subhalo

distributions is a real, physical effect.

While we have shown convergence, it is important to remind ourselves that convergence to an answer does not necessarily imply convergence to the correct answer. Such a concern is raised by van den Bosch et al. (2018) and van den Bosch & Ogiya (2018), who have performed numerical experiments showing that many more particles may be required for robust tracking of subhalo disruption. For example, van den Bosch et al. (2018) find that orbits passing within 10-20% of the virial radius of a host (30-60 kpc for our haloes) may require $\mathrm{N_p} > 10^6$ particles for an accurate treatment. For our simulations, this would correspond to subhaloes with mass $\sim 3 \times 10^9\,\mathrm{M}_\odot$ or $V_{\mathrm{max}} \sim 30\ \mathrm{km\,s^{-1}}$. As can be seen in Figure 2.2, even at this mass scale our simulations still show significant differences between the DMO and `Disk` runs at small radius, and at roughly the same ratios reported for the lower-mass regime. More work will be required to understand the origin of the puzzling differences between our naive understanding of convergence and the detailed work by van den Bosch & Ogiya (2018) to thoroughly understand subhalo mass loss.

2.4.3 Resolution Analysis

Figure 2.12 illustrates the effects of numerical resolution on the V_{max} function for the 'Hound Dog' host halo. The black line shows the results obtained from our fiducial resolution for all objects within 50 kpc (left panel) and 300 kpc (right panel). The red line shows the results obtained from the same halo rerun with 64× fewer particles. The estimated completeness for our high resolution runs used in the main paper is $V_{\mathrm{max}} = 4.5\ \mathrm{km\,s^{-1}}$ (corresponding to subhalos with ~ 170 particles, see 2.2.1). Using $M \propto V_{\mathrm{max}}^{3.45}$, we would expect the lower resolution comparison to be complete to $V_{\mathrm{max}} \simeq 15\ \mathrm{km\,s^{-1}}$ at fixed particle count. We note that the two simulations do indeed begin to systematically differ only below $V_{\mathrm{max}} \simeq 15\ \mathrm{km\,s^{-1}}$, which is indicated by the vertical dotted line. Figure 2.13 shows the radial distributions of

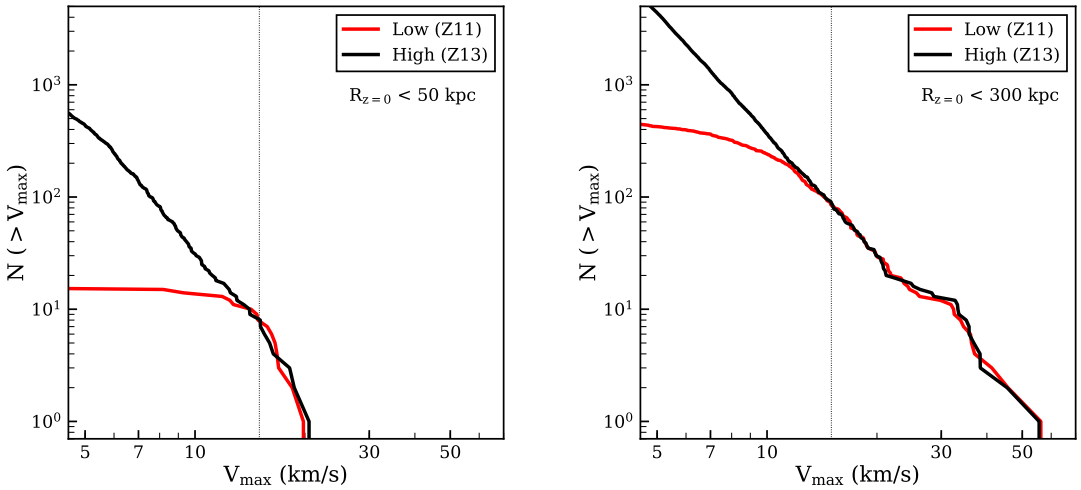

Figure 2.12: Comparison of the subhalo counts of the Hound Dog host halo from our fiducial (High, black) run to a lower resolution run (Low, red), with 64× fewer particles. The left panel shows a cumulative count of all subhaloes above a given $V_{\rm max}$, within 50 kpc of the host center. The right panel is similar but includes subhaloes out to 300 kpc. The vertical dotted line indicates where we would expect convergence ($V_{\rm max} = 15$ km s^{-1}) by scaling our adopted completeness threshold for the fiducial high-resolution runs ($V_{\rm max} = 4.5$ km s^{-1}).

subhaloes with $V_{\rm max} > 15$ km s^{-1} from our high-resolution and low-resolution runs both with (dashed) and without (solid) embedded galaxy potentials. The two resolutions are consistent to within counting errors at all radii. Importantly, the DMO and `Disk` runs appear to be converged down to the same $V_{\rm max}$, which suggests that the differences we see with and without the galaxy potential are real, physical differences and not associated with spurious numerical effects.

2.4.4 Observable consequences

Modulo the above concerns about potential completeness issues, the simulation suite presented here has produced a number of results with potentially interesting implications for interpreting observations.

- The majority of the `Disk` simulations have no subhaloes larger than $V_{\rm max} = 4.5$ km s^{-1}

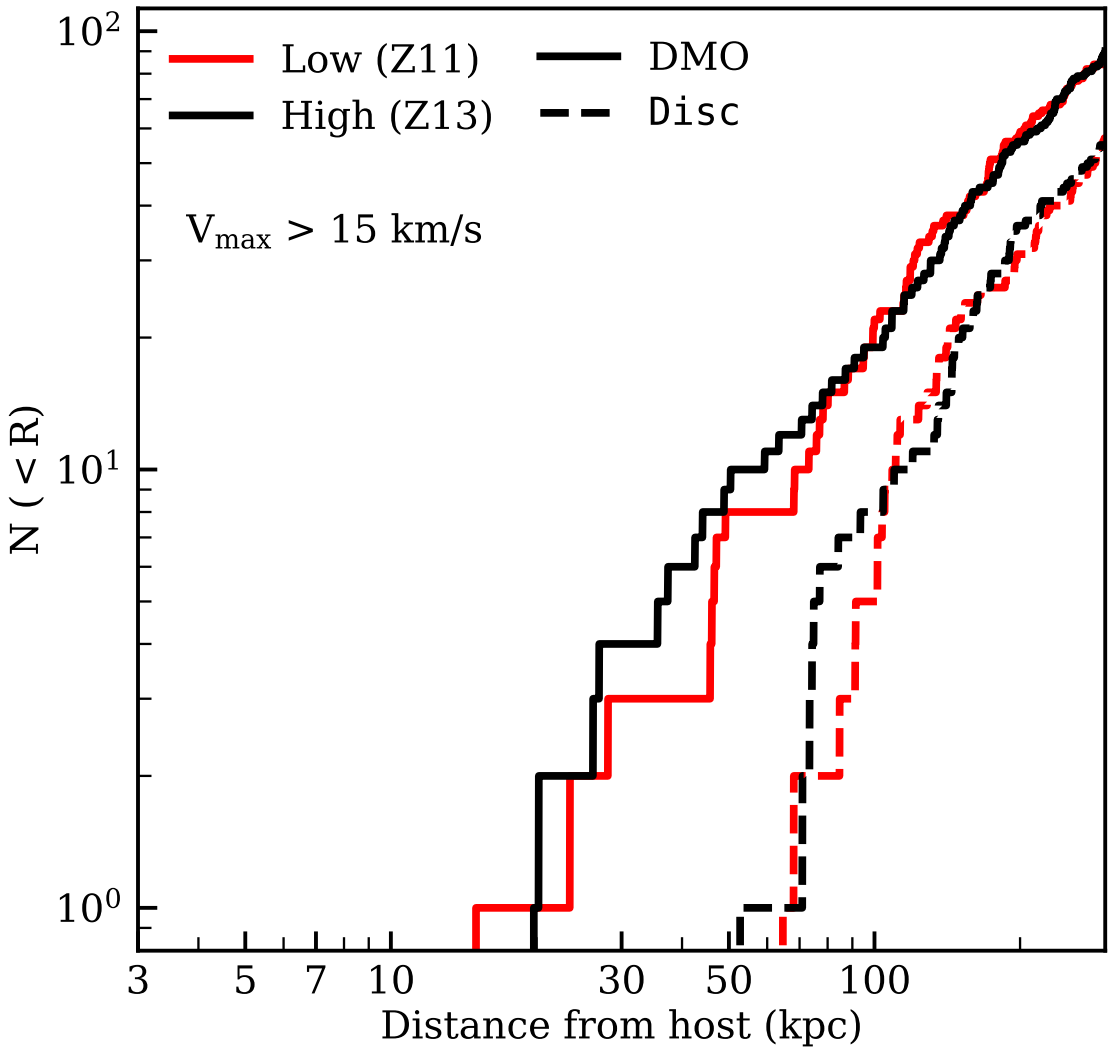

Figure 2.13: Radial radial distributions of subhaloes with $V_{\rm max} > 15$ km s^{-1} for the Hound Dog host halo from the fiducial resolution (High, black) and a run with 64× fewer particles (Low, red). Runs with Milky Way potentials `Disk` are shown as the dashed lines. The counts agree to within expected Poisson variation for both types of runs at all radii.

within 20 kpc (Figure 2.3) and the overall count of subhaloes within this radius remains depressed compared to the DMO runs for several billion years in the past (Figure 2.7). This suggests that local stream-heating signals from dark substructure may be quite rare, even in cold dark matter models without suppressed small-scale power spectra.

- The pericenter distributions of Milky Way satellites derived from *Gaia* data are remarkably similar to the pericenter distributions of subhaloes in the `Disk` runs, while the DMO runs drastically over-predict galaxies with pericenters smaller than 20 kpc (Figure 2.10). This suggests that the Galaxy potential must be considered in any attempt to understand the dynamics and evolution of Milky Way satellites, especially those that exist within the inner ~ 100 kpc of the Milky Way.

- As shown in Figure 2.8, the depletion of inner substructure in the `Disk` runs presents a tension with satellite galaxy counts that is in the opposite sense as that in the Missing Satellites Problem. In order to account for all of the ultra-faint galaxies known within 40 kpc of the Galaxy, we must populate haloes well below the atomic cooling limit ($V_{\rm peak} \simeq 7$ km s^{-1} or $M \simeq 3 \times 10^7\,{\rm M}_\odot$ at infall). The precise value for the minumum $V_{\rm peak}$ varies from host to host, with 9 of our 12 `Disk` runs requiring $V_{\rm peak} = 6.5 - 7.5$ km s^{-1} to explain the counts within 40 kpc. The other three require $V_{\rm peak} = 8.1$, 9.2, and 9.3 km s^{-1}, respectively. There is no apparent trend with host halo mass in the derived minimum values. This issue is discussed in more detail in a companion paper by Graus et al. (2018a).

- If tiny $V_{\rm peak} \simeq 7\,{\rm km\,s^{-1}}$ haloes do host ultra-faint galaxies, as implied by Figure 2.8, this implies the existence of at least ~ 1000 satellite galaxies within 300 kpc of the Milky Way. The number density of such tiny haloes is ~ 100 Mpc^{-3} (e.g. Bullock & Boylan-Kolchin, 2017) in the field, suggesting that there may be $\sim 100,000$ ultra-faint galaxies for every L_* galaxy in the universe.

The aim of this simulation suite is to provide a more accurate set of predictions for dark subhalo properties by including the inevitable existence of a central galaxy potential in calculations of their dynamical evolution. We have focused here on a Milky Way galaxy analog in order to make direct connections to the well-studied population of Milky Way satellites. A similar approach could be used to model satellite subhalo populations for a diverse set of galaxies.

We have shown that the presence of the galaxy significantly changes our expectations for subhalo counts, orbits, and dynamical evolution and that this has a direct bearing on our interpretation of observed satellite galaxy properties as well as efforts to find dark subhalos. Future work in this direction may prove vital in efforts to constrain the nature of dark matter and the physics of galaxy formation on the smallest scales.

Bibliography

Behroozi P. S., Wechsler R. H., Wu H.-Y., 2013a, ApJ, 762, 109

Behroozi P. S., Wechsler R. H., Wu H.-Y., Busha M. T., Klypin A. A., Primack J. R., 2013b, ApJ, 763, 18

Behroozi P. S., Wechsler R. H., Conroy C., 2013c, ApJ, 770, 57

Bland-Hawthorn J., Gerhard O., 2016, ARA&A, 54, 529

Bode P., Ostriker J. P., Turok N., 2001, ApJ, 556, 93

Bonaca A., Hogg D. W., Price-Whelan A. M., Conroy C., 2018, preprint, (`arXiv:1811.03631`)

Bose S., Hellwing W. A., Frenk C. S., Jenkins A., Lovell M. R., Helly J. C., Li B., 2016, MNRAS, 455, 318

Bovy J., Erkal D., Sanders J. L., 2017, MNRAS, 466, 628

Bozek B., Boylan-Kolchin M., Horiuchi S., Garrison-Kimmel S., Abazajian K., Bullock J. S., 2016, MNRAS, 459, 1489

Brooks A. M., Zolotov A., 2014, ApJ, 786, 87

Bryan G. L., Norman M. L., 1998, ApJ, 495, 80

Bullock J. S., Boylan-Kolchin M., 2017, ARA&A, 55, 343

Bullock J. S., Johnston K. V., 2005, ApJ, 635, 931

Bullock J. S., Kravtsov A. V., Weinberg D. H., 2000, ApJ, 539, 517

Carlberg R. G., Grillmair C. J., Hetherington N., 2012, ApJ, 760, 75

Cooper A. P., et al., 2010, MNRAS, 406, 744

D'Onghia E., Springel V., Hernquist L., Keres D., 2010, ApJ, 709, 1138

Despali G., Vegetti S., 2017, MNRAS, 469, 1997

Erkal D., et al., 2018, MNRAS, 481, 3148

Fillingham S. P., Cooper M. C., Wheeler C., Garrison-Kimmel S., Boylan-Kolchin M., Bullock J. S., 2015, MNRAS, 454, 2039

Fitts A., et al., 2017, MNRAS, 471, 3547

Freeman K. C., 1970, ApJ, 160, 811

Fritz T. K., Battaglia G., Pawlowski M. S., Kallivayalil N., van der Marel R., Sohn T. S., Brook C., Besla G., 2018, preprint, (arXiv:1805.00908)

Gaia Collaboration et al., 2018, A&A, 616, A12

Garrison-Kimmel S., Boylan-Kolchin M., Bullock J. S., Lee K., 2014, MNRAS, 438, 2578

Garrison-Kimmel S., et al., 2017a, preprint, (arXiv:1701.03792)

Garrison-Kimmel S., et al., 2017b, MNRAS, 471, 1709

Graus A. S., Bullock J. S., Kelley T., Boylan-Kolchin M., Garrison-Kimmel S., Qi Y., 2018a, preprint, (arXiv:1808.03654)

Graus A. S., Bullock J. S., Boylan-Kolchin M., Nierenberg A. M., 2018b, MNRAS, 480, 1322

Griffen B. F., Ji A. P., Dooley G. A., Gómez F. A., Vogelsberger M., O'Shea B. W., Frebel A., 2016, ApJ, 818, 10

Hahn O., Abel T., 2011, MNRAS, 415, 2101

Hargis J. R., Willman B., Peter A. H. G., 2014, ApJ, 795, L13

Hernquist L., 1990, ApJ, 356, 359

Hopkins P. F., 2015, MNRAS, 450, 53

Horiuchi S., Bozek B., Abazajian K. N., Boylan-Kolchin M., Bullock J. S., Garrison-Kimmel S., Onorbe J., 2016, MNRAS, 456, 4346

Jethwa P., Erkal D., Belokurov V., 2018, MNRAS, 473, 2060

Johnston K. V., Spergel D. N., Haydn C., 2002, ApJ, 570, 656

Kamionkowski M., Liddle A. R., 2000, Physical Review Letters, 84, 4525

Katz N., White S. D. M., 1993, ApJ, 412, 455

Kelley T., Bullock J. S., Garrison-Kimmel S., Boylan-Kolchin M., Pawlowski M. S., Graus A. S., 2019, Monthly Notices of the Royal Astronomical Society, 487, 4409

Kim S. Y., Peter A. H. G., Hargis J. R., 2017, preprint, (arXiv:1711.06267)

Klypin A., Kravtsov A. V., Valenzuela O., Prada F., 1999, ApJ, 522, 82

Koposov S. E., Rix H.-W., Hogg D. W., 2010, ApJ, 712, 260

Kuhlen M., Madau P., Silk J., 2009, Science, 325, 970

Mao Y.-Y., Williamson M., Wechsler R. H., 2015, ApJ, 810, 21

McMillan P. J., 2017, MNRAS, 465, 76

Miyamoto M., Nagai R., 1975, PASJ, 27, 533

Moore B., Ghigna S., Governato F., Lake G., Quinn T., Stadel J., Tozzi P., 1999, ApJ, 524, L19

Navarro J. F., Frenk C. S., White S. D. M., 1997, ApJ, 490, 493

Ngan W., Bozek B., Carlberg R. G., Wyse R. F. G., Szalay A. S., Madau P., 2015, ApJ, 803, 75

Oñorbe J., Garrison-Kimmel S., Maller A. H., Bullock J. S., Rocha M., Hahn O., 2014, MNRAS, 437, 1894

Ocvirk P., et al., 2016, MNRAS, 463, 1462

Okamoto T., Gao L., Theuns T., 2008, MNRAS, 390, 920

Pace A. B., Li T. S., 2018, preprint, (`arXiv:1806.02345`)

Planck Collaboration et al., 2016, A&A, 594, A13

Popping G., et al., 2015, MNRAS, 454, 2258

Riley A. H., et al., 2018, preprint, (`arXiv:1810.10645`)

Rocha M., Peter A. H. G., Bullock J., 2012, MNRAS, 425, 231

Rodriguez Wimberly M. K., Cooper M. C., Fillingham S. P., Boylan-Kolchin M., Bullock J. S., Garrison-Kimmel S., 2018, preprint, (`arXiv:1806.07891`)

Sawala T., Frenk C. S., Crain R. A., Jenkins A., Schaye J., Theuns T., Zavala J., 2013, MNRAS, 431, 1366

Sawala T., et al., 2015, MNRAS, 448, 2941

Simon J. D., 2018, ApJ, 863, 89

Smith R., Flynn C., Candlish G. N., Fellhauer M., Gibson B. K., 2015, MNRAS, 448, 2934

Somerville R. S., 2002, ApJ, 572, L23

Springel V., 2005, MNRAS, 364, 1105

Springel V., et al., 2008, MNRAS, 391, 1685

Stadel J., Potter D., Moore B., Diemand J., Madau P., Zemp M., Kuhlen M., Quilis V., 2009, MNRAS, 398, L21

Thoul A. A., Weinberg D. H., 1996, ApJ, 465, 608

Tollerud E. J., Bullock J. S., Strigari L. E., Willman B., 2008, ApJ, 688, 277

Walsh S. M., Willman B., Jerjen H., 2009, AJ, 137, 450

Wetzel A. R., Tollerud E. J., Weisz D. R., 2015, ApJ, 808, L27

Wetzel A. R., Hopkins P. F., Kim J.-h., Faucher-Giguère C.-A., Kereš D., Quataert E., 2016, ApJ, 827, L23

Wheeler C., Phillips J. I., Cooper M. C., Boylan-Kolchin M., Bullock J. S., 2014, MNRAS, 442, 1396

Zentner A. R., Bullock J. S., 2003, ApJ, 598, 49

Zhu Q., Marinacci F., Maji M., Li Y., Springel V., Hernquist L., 2016, MNRAS, 458, 1559

van den Bosch F. C., Ogiya G., 2018, MNRAS, 475, 4066

van den Bosch F. C., Ogiya G., Hahn O., Burkert A., 2018, MNRAS, 474, 3043

van der Wel A., et al., 2014, ApJ, 788, 28